Bond defects in graphene created by ultralow energy ion implantation

Renan Villarreal[1,†,*], **Pin-Cheng Lin**[1,†], **Zviadi Zarkua**[1], **Harsh Bana**[1], **Hung-Chieh Tsai**[2,3], **Manuel Auge**[4], **Felix Junge**[4], **Hans Hofsäss**[4], **Ezequiel Tosi**[5], **Steven De Feyter**[3], **Stefan De Gendt**[2,3], **Steven Brems**[2], **E. Harriet Åhlgren**[6], **and Lino M. C. Pereira**[1,*]

[1] Quantum Solid State Physics, KU Leuven, 3001 Leuven, Belgium
[2] imec vzw (Interuniversitair Micro-Electronica Centrum), 3001 Leuven, Belgium
[3] Department of Chemistry, Division of Molecular Imaging and Photonics, KU Leuven, 3001 Leuven, Belgium
[4] II.Institute of Physics, University of Göttingen, 37077 Göttingen, Germany
[5] Elettra Sincrotrone Trieste, Strada Statale 14 km 163.5, 34149 Trieste, Italy
[6] Faculty of Physics, University of Vienna, 1090 Vienna, Austria
[†] R.V. and P.-C.L. contributed equally to this work

Abstract.

Ultralow energy (ULE) ion implantation is being increasingly applied to the modification of 2D materials, in particular, for substitutional doping and intercalation of graphene. Implantation-induced defects, whether desired or not, have a strong impact on the properties of graphene. Significant research has been devoted to vacancy-related defects however, disorder induced by ion irradiation in the ULE limit, that is, for energies below the vacancy-formation threshold, remains poorly understood. Here, we focus on that regime and report the formation of defects resulting from the breaking of C-C sp^2 bonds and formation of C-substrate bonds. As a model system we used epitaxial graphene grown on Cu(111) and on Pt(111), subsequently implanted with He, Ne and Ar at energies between 15 eV and 40 eV. The bond defect density is found to increase with increasing energy and atomic number of the implanted element. These findings significantly advance our understanding of disorder induced in graphene by ULE ion implantation, while simultaneously revealing the potential for exploiting such bond defects for physical or chemical functionalization. In particular, these bond defects can be generated with a high degree of selectivity since they occur in the low-energy limit (at least down to 15 eV), significantly below the energies required to form stable vacancies.

Keywords: graphene, disorder, defects, ion implantation, irradiation

Corresponding author. Tel:+32 16323101. E-mail: Renan.Villarreal@kuleuven.be (Renan Villarreal)
Corresponding author. Tel:+32 16320176. E-mail: Lino.Pereira@kuleuven.be (Lino M. C. Pereira)

Final version : https://doi.org/10.1016/j.carbon.2022.12.005

1. Introduction

Ultralow energy (ULE) ion implantation, in which the ions have kinetic energies in the range of tens of eV, is increasingly being explored as a method to functionalize graphene. It has been successfully used to substitutionally dope graphene with N and B [1, 2, 3, 4, 5], P [6], Ge [7], Mn [8, 9] and Au [10]. Recently, ULE ion implantation has also been used to create nanobubbles in graphene down to dimensions of 1 nm radius, in which the highly strained graphene layer holds the implanted (intercalated) noble-gas atoms at extremely high pressures [11]. In addition to the incorporation of the implanted ions in substitutional sites or as intercalated species, ion implantation creates other defects, originating from the collisions between the incoming ion and the atoms in the target material. While disorder may be a detrimental effect when the goal is substitutional doping or intercalation, defects in graphene have useful functional properties of their own [12], by changing the chemical [13] and mechanical [14] properties, or the magnetic behavior [15]. Engineered defects in graphene may also find applications in the fields of hydrogen storage [16, 17], catalysis [18], and capture of organic pollutants [19, 20]. The density of active sites in graphene can be significantly increased not only due to the defects themselves [13, 18, 19] but also due to corrugations and wrinkles that they induce [21, 22, 23]. Here, we report the identification of a type of defect created by ULE ion implantation which has so far not been described, involving broken C-C bonds. Given the flexibility and high degree of control provided by ULE ion implantation [8, 11], these bond defects may in the future be explored as a means to functionalize graphene.

Ion irradiation of graphene can be divided in categories based on the energy regime (from tens of eV, *i.e.*, ultralow energy regime, up to keV) and the type of defects that are formed. For energies of the order of hundreds of eV, a single incoming ion can only displace a few C atoms at most, with larger defects being negligible [24]. Consequently, three types of point defects are typically considered: monovacancy (removal of one C atom), divacancy (removal of two neighboring C atoms) and Stone-Wales (90° in-plane rotation of the bond) [25]. Previous research on ion-irradiated graphene has focused on the 100-1000 eV regime, for example for the formation of nanobubbles in graphene [26, 27, 28]. For energies of the order of keV, besides the three types of point defects that were mentioned above, larger defect complexes (*e.g.*, trivacancies and larger) are predicted to form, as a result of recoil of the carbon atoms [25]. Interestingly, also 1D-like defect complexes were observed in graphene irradiated with 1 keV Ar^+ ions, resulting from interface channeling of the Ar^+ ions, that is, one ion is able to bounce between the graphene layer and the substrate and form 1D arrangements of vacancies [29]. As the energy is decreased from 100 eV, one eventually enters a regime where only single vacancies can be formed [24]. Decreasing further, as the beam energy becomes of the order or lower than the threshold displacement energy ($E_t \approx 22$ eV in graphene [30, 31]), the energy that is transferred to the C atom becomes lower than the minimum required to create a stable C vacancy, and thus no vacancies are expected to form. Although C atoms can be instantaneously displaced, they do not acquire sufficient energy to escape the vacancy that is left behind, and thus recombine with it. Interestingly however, previous work on low-energy ion irradiation of graphene suggests that disorder may in fact accumulate even for ion energies significantly lower than those required to form stable vacancies [32, 11]. This is the case even considering the recent density functional theory molecular dynamics (DFT-MD) corrections to the estimation of the minimum ion kinetic energy [33]. In reference [11], ULE ion implantation was used to create He, Ne and Ar nanobubbles in graphene; despite the low energy (25 eV), below the energy required for vacancy formation, clear accumulation of disorder was observed, revealed by the D band in the Raman spectra. In reference [32], graphene was irradiated using a Ar^+ sputter gun operating at nominal energies of 1 eV up to 200 eV (with an angle of 45° between the ion beam and the sample surface). Interestingly, even at the lowest energies, disorder was still observed. In both cases, the nature of the accumulated disorder remains unclear. Here, we focus specifically on this regime, below the threshold displacement energy. We identify a type of defect that is formed as a result of the collision between an impinging ion and the C atoms in the graphene layer, that is, the breaking of C-C bonds and formation of bonds between graphene and the substrate onto which it is supported. We use noble gas elements (He, Ne and Ar) as model implanted species; their inert nature allows us to study the bond defects without interference from more reactive elements (such as Mn).

2. Experimental and computational details

Our samples consist of epitaxial graphene grown by chemical vapor deposition (CVD) on epitaxial Pt(111) and Cu(111) thin films grown on sapphire(0001) substrates [34, 35]. The samples were implanted with noble gas ions (He, Ne and Ar), with kinetic energies between 15 eV and 40 eV, with perpendicular incidence with respect to the surface. The samples were subsequently studied in the as-implanted state, using scanning tunneling microscopy (STM), Raman spectroscopy and X-ray photoelectron spectroscopy (XPS). These experiments were combined with MD simulations. Additional details on these experimental and computational methods are given in the remainder of this section.

In order to minimize sample degradation (water intercalation [36, 37] and substrate oxidation [38]), the exposure to ambient was kept to a minimum, by storing the samples in a vacuum desiccator (base pressure $\approx 10^{-2}$ mbar). For transportation between different laboratories (between growth, implantation and multiple characterization steps), the samples were sealed in plastic bags at low vacuum (800 mbar), which significantly slows down the process of substrate oxidation during the transportation times (of the order of one day). The samples were only exposed to the atmosphere when they were being manipulated (mounted/dismounted) between different setups, with a typical exposure time of the order of a few minutes per manipulation. This ensures a clean graphene surface (*i.e.*, with a minimal amount of surface adsorbates) before the implantation (cf. STM topographies of pristine after short time air exposure:

Gr/Pt(111) in figure 4a,d and Gr/Cu(111) in figure S4a).

2.1. CVD growth of graphene

Two inch polished Czochralski grown sapphire wafers cut along the c-plane with <0.1° miscut were used to prepare Al_2O_3 template wafers. The as-received wafers were first cleaned in a 3:1 volume ratio of the acid mixture of H_2O_4:H_3PO_4 at 180 °C for 20 min, followed by an ultrapure water rinse for 3 min. Immediately after the cleaning process Pt and Cu films were grown. For Pt, a 500 nm thick film was evaporated on the sapphire wafer by electron-beam deposition (Pfeiffer PLS 580) while keeping the temperature of the wafer at approximately 550 °C on a heated chuck. The base pressure was 4×10^{-7} mbar. The deposition rate was controlled at 1 Å s^{-1} by a quartz crystal rate monitor. For Cu films, the cleaned sapphire wafers were placed in a Nimbus 310 sputtering setup with a base pressure of 4×10^{-6} mbar. Substrates were placed by using a 200 mm Si pocket wafer, and sputtering was performed at room temperature for 173 s (21 passes under target) at 6×10^{-3} mbar Ar pressure. The Cu deposition rate was calibrated and corresponds to a rate of about 29 Å s^{-1}. The applied power was 3000 W, and the throw distance was ∼50 mm. The growth of CVD graphene on the Pt films was performed in a cold wall CVD reactor (Aixtron Black Magic 6 inch) at a pressure of 750 mbar, a temperature of 1100 °C, and with a gas mixture of 9 sccm CH_4 and 800 sccm H_2. Before and after the 40 min growth period, the reactor was ramping up and cooling down in a H_2 environment. The graphene growth process on the Cu films has been optimized by taking into account oriented monolayer growth and the low Raman D peak. The growth conditions were 5000 sccm Ar, 125 sccm H_2, 0.3 sccm CH_4 at a pressure of 750 mbar close to the melting point of Cu. The growth time was 30 min, while ramp-up and ramp-down were performed in a mixture of Ar and H_2.

2.2. Ultralow energy ion implantation

Ultralow energy (ULE) ion implantation was performed at room temperature by electrostatic deceleration of the ion beam ($^4He^+$, $^{22}Ne^+$, $^{40}Ar^+$) from 30 keV to 25 eV, to a fluence of 1×10^{15} ions per cm^2 (fluence rate of the order of 2×10^{12} $cm^{-2}s^{-1}$) measured by integration of the electric current on sample during implantation [39]. The implantation chamber is kept under ultra-high vacuum (UHV, with a base pressure $\sim 5 \times 10^{-9}$ mbar), in order to minimize energy-loss contributions to the energy spread of the ions and to minimize surface contamination (*e.g.*, with hydrocarbons) during the implantation.

2.3. Scanning tunneling microscopy

We acquired the STM micrographs in UHV (base pressure $\sim 10^{-11}$ mbar) using a Unisoku USM1000, an Omicron LT STM and a Unisoku USM1500. We used electrochemically etched W tips and cut Pt-Ir tips. The tip oxide from the W tips is first removed by flash annealing. Consequently, the tips were characterized by scanning the Au(111) surface. All topographies were acquired in constant tunneling current ($I_{tun.}$).

2.4. Raman spectroscopy

Raman spectra were measured by a confocal Raman microscope (Monovista CRS+, S&I GmbH) equipped with a 532 nm Nd:YAG laser. The laser was directed onto the sample surface through an objective (OLYMPUS, BX43 50×, numerical aperture 0.75), with the maximum laser power remaining below 1 mW to avoid laser-induced modification. All the measurements were obtained in ambient conditions at room temperature.

2.5. X-ray photoelectron spectroscopy

The XPS measurements on graphene/Pt(111) (Gr/Pt) were performed at the SuperESCA beamline at Elettra synchrotron in Trieste. All the spectra were acquired in UHV (base pressure $\sim 10^{-10}$ mbar), and the samples were placed in the normal emission (NE) configuration, with respect to the hemispherical analyzer. The photon energies were chosen by optimizing the photoelectric cross section and the surface sensitivity, where the C 1s, O 1s, and Pt 4f core-level spectra were acquired at photon energies of 400, 650, and 200 eV, respectively, with energy resolution always below 150 meV. The binding energy scale has been calibrated with the Fermi level of the metal substrate. The high-resolution core-level spectra were fitted with Gaussian-Lorentzian sum functions (to approximate a Voigt profile) and a linear background.

The XPS measurements on graphene/Cu(111) (Gr/Cu) were performed using a laboratory setup equipped with a Mg K_α X-ray (XR4 Twin Anode X-ray source, non-monochromatic) and an *Alpha 110* hemispherical analyzer. The spectra were acquired with an energy step of 0.2 eV and energy resolution of $\sim$ 1 eV, in UHV (base pressure $\sim 10^{-8}$ mbar), at room temperature, with a beam spot of $\sim$ 5 mm in diameter (sampling area).

2.6. Molecular dynamics simulations

The dynamics of the ultralow energy irradiation of Gr/Pt(111) with He/Ne/Ar was modeled employing classical molecular dynamics with the PARCAS code. The (111)-surface was cut into a Pt bulk of 9×7 nm yielding a slab thickness of about 2 nm totalling 9180 atoms. A commensurate Gr sheet with 2552 atoms was set above the surface and relaxed in a canonical ensemble to a local energy minimum at 0 K returning the distance of about 0.38 nm above the Pt(111) surface. The interatomic interactions between Pt-Pt and Pt-C were modeled with the Albe potential [40] and the C-C interactions with bond-order potential by Brenner [41] smoothly joined to a repulsive term at small atomic separations [42]. The ion-C interactions were modeled with the universal repulsive potential [42]. Each ion was placed at a distance of about 1 nm above the pristine Gr sheet with an impact point randomly sampled from an irreducible area of the hexagonal lattice. A total of 1000 impacts per ion/energy was simulated to allow representative probabilities for various types of events to occur. The minimum detection limit was therefore 0.1 %. Due to the ultralow energies the energy transfer was fully nuclear and the charge state of the ion was not considered. Each impact was simulated for 400 fs allowing the system to reach a local energy minimum after the impact before analysing the system. Periodic boundary conditions were introduced in the directions perpendicular to the ion to mimic infinite surface with heat dissipation at the edges modeled with the Berendsen thermostat [43].

3. Results and Discussion

In this section, we focus first on the Gr/Pt system, presenting and discussing the Raman, STM and XPS data, as well as the MD simulation results. In this first part (section 3.1), we are only able to qualitatively discuss the Raman spectroscopy results, due to the low signal-to-background ratio characteristic of Gr/Pt. The Raman bands, particularly the *G* and *2D* bands, are known to be weaker for graphene on a substrate compared to suspended graphene, especially for metallic substrates [44], due to electromagnetic screening and hybridization effects. Compared to suspended graphene, the intensity of the *G* and *2D* bands in Gr/Cu is suppressed to approximately 14% and 7%, respectively; in Gr/Pt the suppression is significantly stronger, to 2% and 0.06% respectively. Due to the low signal-to-background ratio, the analysis (fitting) of the Gr/Pt data is highly sensitive to how the background is modeled, making it difficult to extract reliable quantitative information. For a quantitative Raman spectroscopy study, we used Gr/Cu, presented in section 3.2.

3.1. Bond defects in implanted graphene/Pt

Three Raman bands are typically used for the characterization of disorder in graphene: *D*, *G* and *2D* bands. The *G* and *2D* bands are characteristic of a well-ordered graphene lattice; the *D* band is associated with disorder. Figure 1 shows Raman spectra for Gr/Pt, pristine and implanted with the three noble gas elements, at 15 eV and 25 eV. While the pristine sample and the samples implanted with He show only the *G* and *2D* bands typical of Gr/Pt, without a *D* band, the samples implanted with Ne and Ar show the emergence of a *D* band, which increases in intensity or area with increasing energy and atomic number of the implanted element. As mentioned above, reliable quantitative analysis is hampered by the low signal-to-background ratio characteristic of Gr/Pt. Instead, we performed a more quantitative Raman spectroscopy study on Gr/Cu, which we present in section 3.2. In the present section, we first study the Gr/Pt system in more detail.

It can be seen in the Raman data on Gr/Pt that the emergence of a *D* band is accompanied by a broadening of the *G* band and a weakening of the *2D* band, both of which are indicative of increasing disorder (as also discussed in more detail based on the

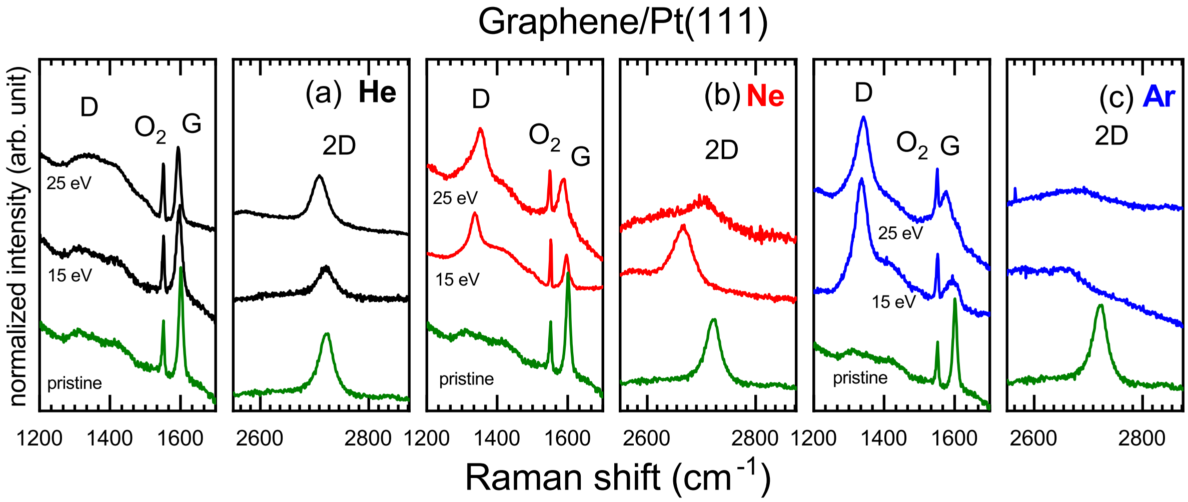

Figure 1. Raman spectra of Gr/Pt, pristine and implanted with noble gases: (a) He, (b) Ne, (c) Ar, at 15 eV and 25 eV. The intensity is normalized to the intensity of the oxygen related band at 1550 cm^{-1}. The positions of the *D*, *G*, and *2D* bands of graphene are indicated, as well as the atmospheric O_2 band.

Gr/Cu data). The creation of disorder at such low ion energies (down to 15 eV) is rather unexpected. The defects that are typically considered in the context of ion irradiation of graphene are of the vacancy-type, that is, when an impinging ion transfers enough energy to the C atom in the graphene lattice so that the C atom is displaced, leaving behind a stable C vacancy. By simple kinematics (conservation of kinetic energy and momentum) [45], we can estimate the minimum energy E_{min} that the ion beam must have in order to produce a stable vacancy, based on the C threshold displacement energy (E_t, *i.e.*, minimum energy that must be transferred to the C atom to create a stable C vacancy) and the maximum energy transferred by an impinging ion (in a head-on collision), using the following equation:

$$E_{\mathrm{min}} = E_t \frac{(M_{\mathrm{ion}} + M_{\mathrm{C}})^2}{4 M_{\mathrm{ion}} M_{\mathrm{C}}}, \tag{1}$$

where M_{ion} and M_{C} are the atomic masses of the impinging ion and of C, respectively. Taking the typical value of $E_t \approx 22$ eV [31] for graphene gives E_{min} values of 29 eV, 23 eV and 31 eV for He, Ne and Ar, respectively. Since we observe significant disorder for Ne and Ar at much lower energies (down to 15 eV), this suggests that a different type of defect (not vacancies) is involved.

In order to gain insight on the nature of this unexpected low-energy disorder, we performed MD simulations of He, Ne and Ar ions implanted into graphene on a Pt(111) surface. Figure 2 shows examples of defects that are indeed formed without the effective removal of C atoms (vacancy formation). The impinging atom induces a significant displacement of one or more C atoms, towards the Pt surface, resulting in the breaking of C-C sp^2 bonds and formation of bonds between the displaced C atoms at Pt atoms at the interface. Although these displaced C atoms are no longer within the graphene

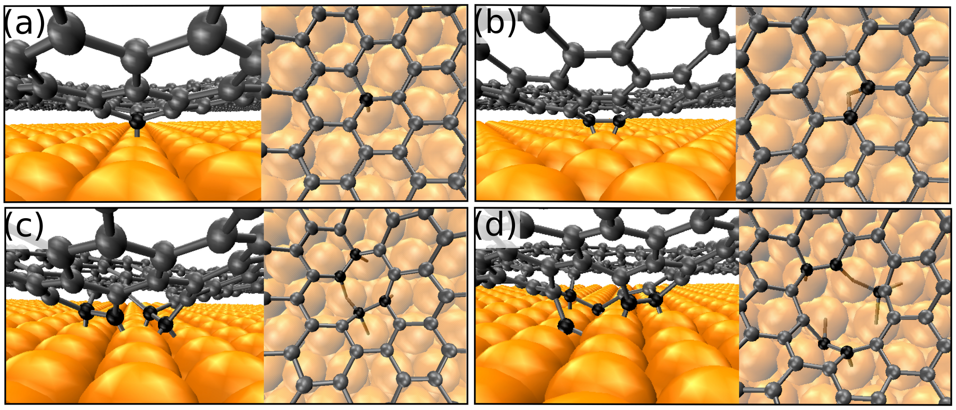

Figure 2. Snapshots of MD simulations after ion impact depicting the bond defects formed when the C-C sp^2 bonds (grey) are broken and the displaced C atoms (black) form new bonds with the Pt surface (orange). Examples with side and top view of (a) one bond defect (b) two bond defects (c) four bond defects and (d) five bond defects after a single impact. The Pt surface is transparent in the top view for visibility.

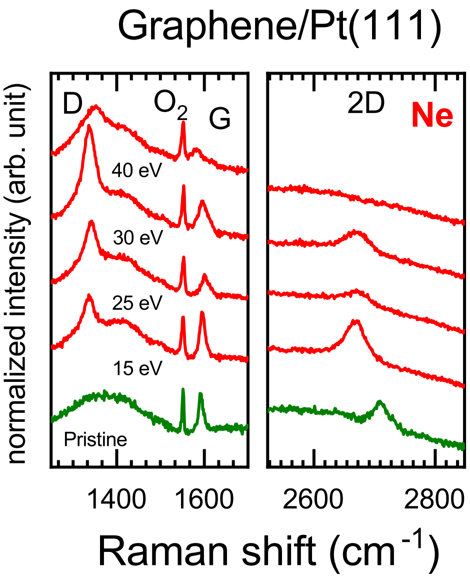

Figure 3. Raman spectra of Gr/Pt, implanted with Ne at 15 eV, 25 eV, 30 eV and 40 eV. The intensity is normalized to the intensity of the oxygen related band at 1550 cm^{-1}. The positions of the *D*, *G*, and *2D* bands of graphene are indicated, as well as of the atmospheric O_2 band.

plane, they are still bound to C atoms from the graphene layer. Therefore, they are not classified as vacancies, but instead as *bond defects*. We can further classify them by how many C-Pt bonds are created by one single impinging atom, from 1 to 6 (*i.e.*, a full C hexagon). These results are compiled in figure 2: the average number of C-Pt bonds formed per impinging atom; the probability of an impinging atom forming any number of C-Pt bonds. More detailed statistics, that is, the specific probability for any n number of C-Pt bonds, are given in the supplementary material section 1. For a given energy, both parameters increase with atomic number of the implanted element. The fact that a similar evolution is observed in the disorder as characterized by Raman spectroscopy supports the notion that the latter is indeed due to the formation of such bond defects. Moreover, for all three elements, both parameters increase monotonously up to 30 eV, showing a saturating behavior as the energy is increased to 40 eV (with a slight decrease at 40 eV). A similar trend is also observed in the Raman data (cf. figure 1 for all three elements at 15 eV and 25 eV and figure 3 for Ne between 15 eV and 40 eV). A more quantitative Raman study was performed on Gr/Cu (cf. section 3.2), showing these trends even more clearly, that is, increase in disorder with increasing atomic number of the implanted atom, as well as with increasing energy.

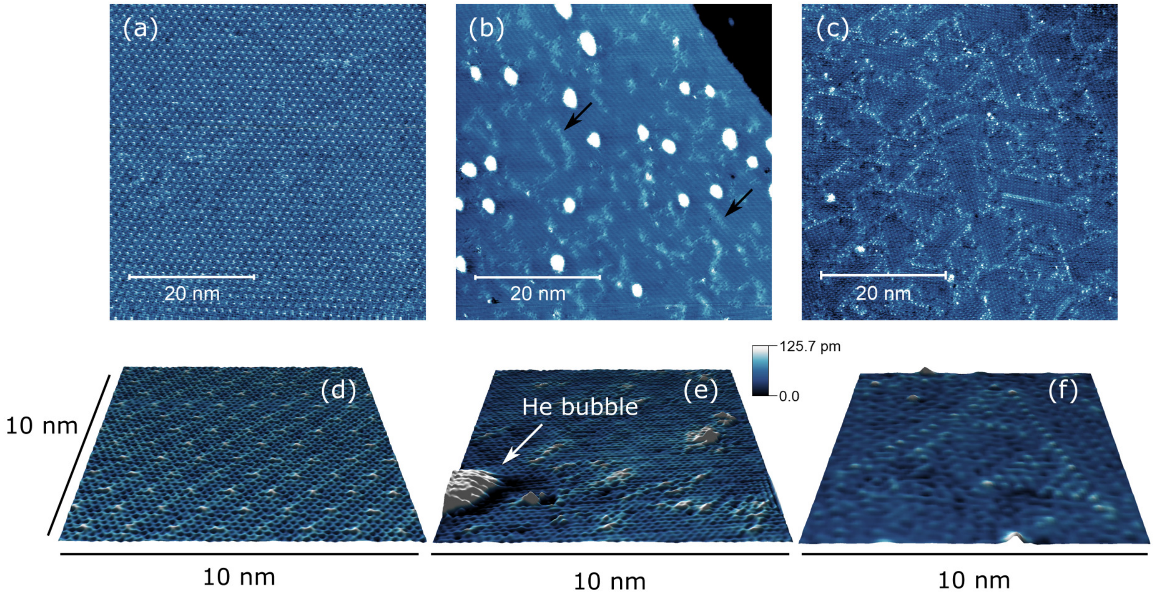

Figure 4. STM micrographs showing: (a,d) The moiré periodicity in pristine Gr/Pt (measured at RT with V_{sample} = -300 mV, $I_{tun.}$ = 200 pA); (b,e) As-implanted 15 eV He Gr/Pt (measured at RT with V_{sample} = -100 mV, $I_{tun.}$ = 100 pA); (c,f) 200 °C annealed 15 eV Ne implanted Gr/Pt (measured at 78 K with V_{sample} = -400 mV, $I_{tun.}$ = 40 pA). Black arrows indicate 1D-like bond defects structures.

STM shows features that can be attributed to the bond defects described above. In figure 4, we compare the surface of pristine graphene to those of He and Ne implanted graphene (the latter after 200 °C annealing). In the case of pristine graphene, we see the moiré superstructure resulting from the interference between the lattices of graphene and Pt(111). For He and Ne implanted graphene, in addition to the graphene nanobubbles [11], the moiré superstructure appears disturbed, and additional defects are observed. Although these perturbations on the local density of states (LDOS) of the surface appear as protrusions, we interpret them as due to the LDOS associated with the formed C-Pt bonds, in which the C atoms are in fact shifted downwards (towards the Pt surface, as depicted in figure 2). A similar effect in the LDOS (appearing as a protrusion rather than a depression, even though the involved C atoms are shifted downwards), has been observed for C-Pt bonds in the neighborhood of single carbon vacancies in graphene/Pt [46, 47], when the C-Pt bond involves the C π-orbital rather than the σ-orbitals. Such a scenario, in which the C-Pt bonds formed in our samples involve the C π-orbital, would also explain the difficulty in observing these defects using STM, as it seems to require tip functionalization, as discussed in more detail in section 2.2 of the supplementary information. Our STM data show that these defects tend to be agglomerated in 1D-like structures, as shown in the as-implanted case for He in figure 4b,e, with some defects appearing isolated but most being agglomerated in 1D-like structures. This agglomeration and self-organization is even more clear after thermal annealing at 200 °C as shown for Ne implanted graphene in figure 4c,f. This annealing was required to improve the stability of the tunnel junction when measuring Ne implanted samples. Without annealing, strong instabilities are observed (figure S3), most likely due to disorder and surface contamination. Interestingly, in addition to providing higher quality data due to a more stable tunnel junction, the defects after annealing appear to be ordered in straighter and longer line structures (compared to the as-implanted He case). In several areas, these 1D structures wrap around in triangular shapes, that is, following a 3-fold symmetry. This observation is consistent with bond defects that are already somewhat mobile at room temperature, allowing some degree of self-organization; increasing the temperature to as little as 200 °C leads to further self-organization into more ordered structures. This further self-organization likely follows the symmetry of the Gr-Pt interface. This agglomeration effect suggests that isolated bond defects are metastable, experiencing diffusion and self-assembly into more stable extended (1D-like) defects, within a short time scale, that is, during or immediately after the implantation at room temperature, before further characterization. It is also possible that a fraction of the isolated defects are dynamically annealed, that is, that the sp^2 C-C bonds are restored within that short time scale. We return to this point below, when discussing the more quantitative Raman spectroscopy study on Gr/Cu (cf. section 3.2).

While bond defects are formed in the whole energy range that was considered (15-40 eV), our MD simulations in the high-energy end (40 eV) also predict the formation of defects that can be classified as vacancies. These events were analysed by filtering the forward-sputtered C atoms based on their coordinates and bonding order with other C atoms. Further manual checks were employed to cases where this automatic filtering was uncertain. Backwards sputtering was not detected. Taking this definition, we obtain a probability for vacancy formation, at 40 eV, of 0.001 for He and of 0.01 for Ne. This small formation probability compared to the bond defects (figure 5b), together with the fact that we do not find clear evidence of vacancy defects in our STM data, further support the notion that disorder in this low-energy regime is dominated by bond defects. Moreover, even if vacancies are formed, they may experience diffusion and trapping in defective regions or dynamic annealing, which would further decrease their concentration or detectability with STM.

These broken (dangling) bonds are highly reactive, and are thus expected to lead to the formation of bonds between the damaged graphene and nearby atoms or

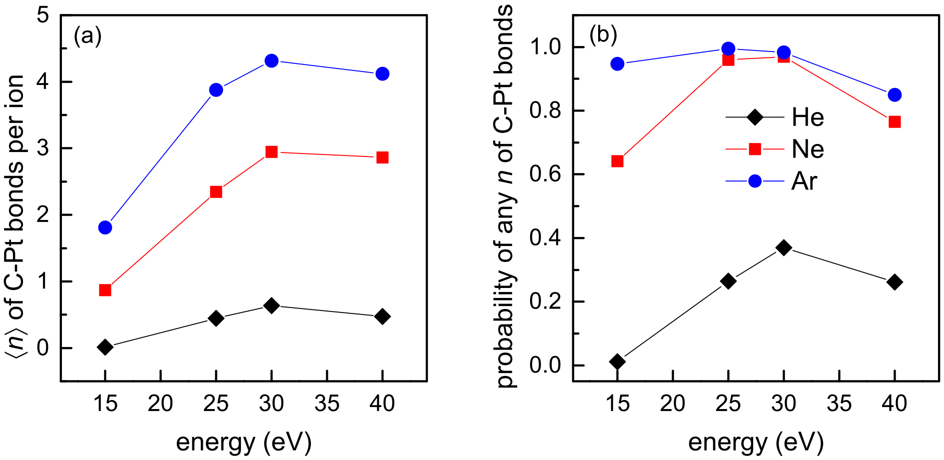

Figure 5. Statistics on the bond defects simulated by MD, as a function of kinetic energy of the impinging atom: (a) Average number of C-Pt bonds formed per impinging ion; (b) Probability of an impinging ion to form any number of C-Pt bonds.

molecules, either from the substrate surface (as in our MD simulations) or from the atmosphere (*e.g.*, adsorbed hydrocarbons). Although our XPS measurements on Gr/Pt (section 2.1 of the supplementary material) and Gr/Cu (subsections 3.3 and 3.4 of the supplementary material) do show an increase in adsorbed hydrocarbon contamination in the implanted samples (which is also consistent with the increased difficulty in obtaining stable tunneling conditions for the STM measurements), this increase is largely independent of the implanted species, contrary to the disorder that we detected using Raman spectroscopy, which increases with increasing atomic number of the implanted ion (for Gr/Pt above in the present section, and for Gr/Cu in the following section 3.2). We therefore conclude that these bond defects are mostly passivated via formation of bonds with the substrate (as predicted by our MD simulations), which in turn is the origin of the disorder detected with Raman spectroscopy. The formation of carbon-substrate bonds has also been observed for vacancy defects in ion-irradiated Gr/Pt [46] and Gr/Ir [48].

3.2. Quantitative Raman spectroscopy study on Gr/Cu

In this subsection, we describe a more quantitative Raman spectroscopy study, taking Gr/Cu instead of Gr/Pt, since the graphene Raman bands are significantly less attenuated [44], as mentioned above. This results in a higher signal-to-background ratio, and therefore less sensitivity to how the background is modeled. In figure 6, the Raman spectra are shown as a function of energy, for the three implanted noble gas elements.

In order to quantify the evolution of the Raman spectra as a function of implantation energy, the following parameters of the Raman bands (*D*, *G*, *2D* bands) were determined: position (ω), FWHM (Γ), intensity (I), and integrated area (A). These parameters were obtained by fitting the spectra. A linear background was

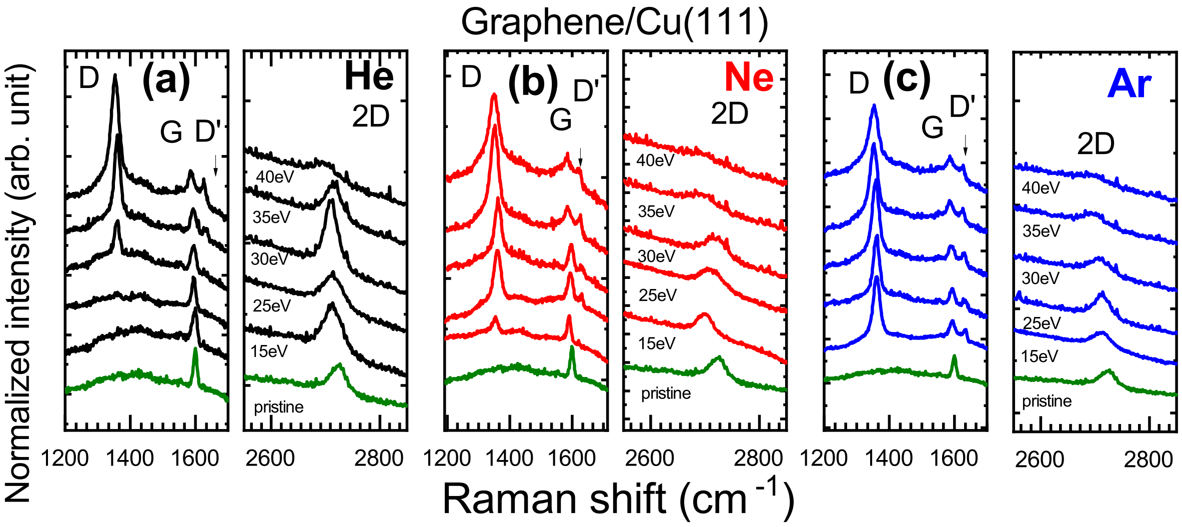

Figure 6. Raman spectra for Gr/Cu, pristine and implanted with He, Ne and Ar, for implantation energies between 15 eV and 40 eV. The intensity of the spectra is normalized by the intensity of the corresponding *G* bands. The implantation energies and the positions of the *D*, *G*, *D′* and *2D* bands of graphene are indicated.

subtracted and the Raman bands were subsequently fitted with a Lorentzian lineshape. Due to the limitations imposed by the Cu background, the spectral contribution of amorphous carbon (that starts to form in *stage 2* of the *amorphization trajectory* [49]) was not taken into account in the analysis as in references [50, 51]. This amorphous carbon background consists of two broad bands with FWHM above 150 cm^{-1}. When measuring with a laser wavelength of 532 nm (as the data presented here), these two bands would be expected at 1275 cm^{-1} and 1520 cm^{-1} [51]. Apart from the *D* band, another disorder-induced Raman band, the *D′* band ($\omega_{\mathrm{D'}} \approx 1630\ cm^{-1}$), can be identified as a single peak on the higher binding energy side of the *G* band (figure 6). The *D′* band emerges around an implantation energy of 30 eV for He and 25 eV for Ne, while for Ar it is present down to the lowest energy (15 eV). The intensity ratio of the two disorder induced Raman bands, that is, $I_{\mathrm{D'}}/I_{\mathrm{D}}$, has previously been used to identify the type of disorder, including grain boundaries, sp^3 defects, and vacancies [52]. However, in our data, considering the low intensity of the *D′* band and the detrimental effect of the Cu-related background, it is less appropriate to extract such detailed information.

In the following paragraphs, we briefly analyze the peak positions of the *G* and *2D* bands and the FWHM of the *G* band, and then discuss the disorder quantification in more detail based on the ratios of *D*-to-*G* bands. Interestingly, although Gr/Cu allows for a more quantitative analysis of the implantation-induced disorder, compared to Gr/Pt, the characterization of these defects using STM is more challenging, as described in section 3.1 of the supplementary information.

3.2.1. Peak position of the G *and* 2D *bands.* Figure 7 shows the peak position of the *G* and *2D* bands (denoted as ω_G and ω_{2D}, respectively), as a function of

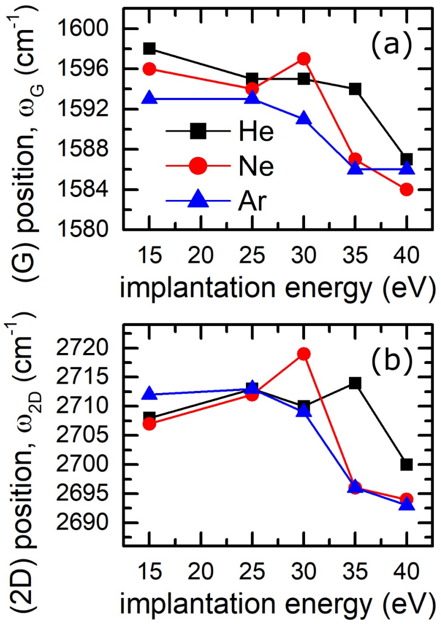

Figure 7. Position of (a) the *G* band and (b) the *2D* band, as a function of the implantation energy (from 15 eV up to 40 eV), for the three noble gases (He, Ne, Ar). For pristine Gr/Cu, $\omega_G = 1600$ cm^{-1} and $\omega_{2D} = 2720$ cm^{-1}. The standard deviation for ω_G is $\sim \pm$ 2.2 cm^{-1}; for ω_{2D} it is $\sim \pm$ 6 cm^{-1} (determined by measuring multiple spots on the samples).

implantation energy, for the three noble gases. At low energy, both ω_G and ω_{2D} show an approximately constant redshift in comparison to pristine Gr/Cu (with $\omega_G = 1600$ cm^{-1} and $\omega_{2D} = 2720$ cm^{-1}). Above a certain energy, a significant increase in redshift is observed with increasing implantation energy. The onset of that redshift occurs at 40 eV for He, and at 35 eV for Ne and Ar. For n-doped graphene (Gr/Cu), the redshift of the *G* band can result from the downshift of the Fermi level (E$_F$) [53], which may result from weaker graphene-Cu interaction (*i.e.*, less charge transfer from Cu to graphene) or oxygen absorption (*i.e.*, as a source of hole doping) [54]. Although a decrease in charge doping may be partly responsible for the redshift of the *G* band observed in our samples, that still does not explain the redshift of the *2D* band. Apart from doping, also strain can induce the shift of the *G* and *2D* bands; in particular, a simultaneous redshift of the *G* and *2D* bands is associated with tensile strain [55]. In the case of Gr/Cu, it is known that tensile strain can be induced upon the oxidation of Cu(111) [56, 57, 58]. However, no trace of Cu oxidation was observed on our implanted Gr/Cu samples, even for Ar at 40 eV (cf. XPS spectra in figure S7 and Raman spectrum in figure S8), that is, where the redshift is maximized. Therefore, the tensile strain in our samples is likely related to the disorder induced by implantation: the formation of bonds between the C atoms in graphene and the Cu atoms at the interface, which results in a local stretching of the C-C sp^2 bonds near the bond defects (figure 2 for Gr/Pt). A similar effect has also been described for vacancy defects created by ion irradiation of CVD grown Gr/Ir(111) [48].

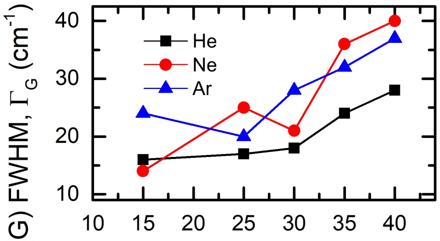

Figure 8. *G* band FWHM, as a function of the implantation energy (from 15 eV up to 40 eV), for the three noble gases (He, Ne, Ar). The standard deviation for the FWHM of the *G* band is $\sim \pm$ 1.4 cm^{-1} (determined by measuring multiple spots on the samples).

3.2.2. Full width at half maximum of the G *band.* The FWHM of the Raman bands is inversely proportional to the lifetime of the photo-excited electrons [59]. Among all the Raman active bands, the FWHM of the *G* band is commonly used as a measure of disorder, as it is sensitive to all kinds of disorder [49, 60]. Likewise, the FWHM of the *2D* band also evolves as a function of disorder concentration. However, considering the low intensity of the *2D* band and the relatively high spatial variation (variation of the intensity across the sample surface, even on pristine Gr/Cu), only the FWHM of the *G* band is analyzed in more detail here. Figure 8 shows the evolution of the FWHM of the *G* band (denoted as Γ_G). The Γ_G shows small variations at low energy and a noticeable increase from approximately 30 eV. It is worth noting that Γ_G of pristine Gr/Cu is $\approx$ 12 cm^{-1}, which is lower than all implanted cases presented here. Even the implantation at 15 eV induces some degree of broadening, although minimal for He and Ne.

3.2.3. D *band versus* G *band ratio.* Two types of ratios, that is, peak intensity ($I_{\mathrm{D}}/I_{\mathrm{G}}$) and peak integrated area ($A_{\mathrm{D}}/A_{\mathrm{G}}$), can be used as indicators to evaluate the amount of disorder [49, 24, 60, 5]. For graphene with low disorder density (at the beginning of *stage 1* of the *amorphization trajectory*), intensity and integrated area ratios are expected to give similar results, since the FWHM remains approximately constant (cf. figure 8) [61]. However, for graphene with high disorder concentration, the intensity ratio becomes more sensitive than the integrated area ratio. In the regime of high disorder (starting from the end of *stage 1* of the *amorphization trajectory*), with increasing disorder, the intensity of the Raman bands decreases and the FWHM increases, which makes the integrated area less sensitive to variations in structural disorder. Here, we present both intensity and area ratios, for completeness.

As can be seen in figure 9, both the intensity and the integrated area ratios show a three-region evolution. For Ne, all three regions can be observed, while for He and Ar, only two. At the lowest energies, which we will refer to as region A (more clearly observed for He), the ratio remains at a small constant value (below the detection limit). At higher energies, in a region that we will refer to as B (clearly observed on both He and

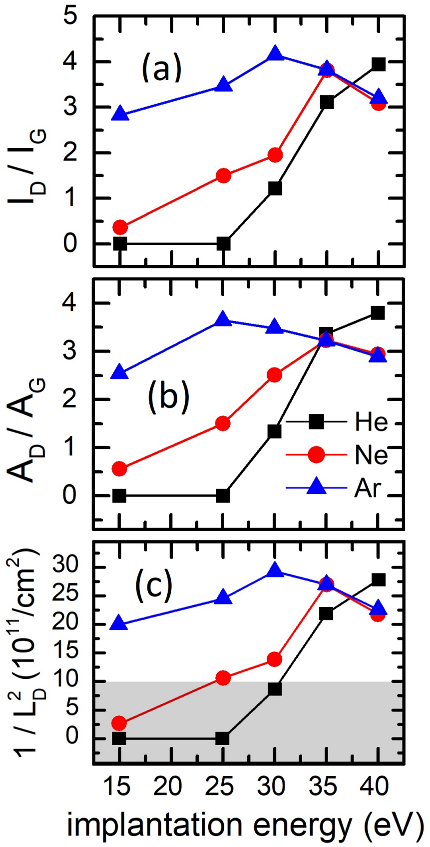

Figure 9. *D versus G* ratio of (a) the intensity and (b) the integrated area, as a function of the implantation energy. The standard deviation of the intensity ratio is ∼ ± 0.2; the standard deviation of the integrated ratio is ∼ ± 0.3 (determined by measuring multiple spots on the samples). (c) $1/L_D^2$ (as an estimation of the defect concentration) calculated using equation 2. The grey area marks the regime where equation 2 is valid, that is, in which the average distance between point defects (L_D) $\geq$ 10 nm.

Ne), the ratio increases with increasing implantation energy, indicating that disorder is accumulating without significant coalescence [24]. The transition between regions A and B (around 25-30 eV for He and Ne) indicates a significant increase in the defect formation rate. Finally, at the highest energies, in a region that we refer to as C (observed for Ne and Ar), the ratio starts to decrease with increasing implantation energy, as a result of the coalescence of the disordered areas [24]. The transition (maximum value of the ratios) between regions B and C occurs around 30-35 eV for Ne and Ar. Such transition marks the onset of the coalescence between disordered areas, which also corresponds to the transition between *stage 1* and *stage 2* of the *amorphization trajectory*, that is, that amorphous carbon starts to form in graphene [49]. In short, region A and B fall within *stage 1* of *amorphization trajectory*, while region C within *stage 2* [49]. It is noteworthy that in the case of He, only region A and B can be identified, with the *D* band being absent for implantation energies of 25 eV and below; the *D* band emerges at 30 eV, and increases up to the highest energy used here (40 eV), suggesting that region C (observed for Ne and Ar) would eventually emerge at higher energies. Although the substrate is likely to play an important role on the bond-breaking mechanism and the formation of C-substrate bonds, our Raman data for Gr/Pt and Gr/Cu as well as our MD simulations for Gr/Pt show the same qualitative trends: increase in disorder with increasing energy and atomic number of the impinging element. Interestingly, however, the amount of surface contamination is largely independent of the implanted species. In particular, for an implantation energy of 25 eV, whereas the ratio of the D band versus G band shows a strong dependence on implanted ion (vanishingly small for He, near maximum for Ar, and intermediate for Ne - figure 9), the amount of surface contamination detected using XPS is essentially constant (section 3 in supplementary information). Therefore we conclude that, although the surface modification induced by the ion implantation increases the surface reactivity of graphene, leading to a measurable increase in the amount of surface contamination, the latter does not scale with the amount of disorder. In other words, surface functionalization with contaminants such as hydrocarbons is unlikely to be the origin of the modifications in the Raman spectra (in particular the emergence of the D band), which we attribute instead to the bond defects predicted by our MD simulations. These bond defects are nevertheless likely to contribute to the increase in surface contamination by increasing the surface reactivity; not only acting as active sites themselves, but also due to the increased surface activity associated with the surface corrugations [21, 22, 23] that the bond defects induce (cf. figure 4e).

The ratio of the D versus G bands can also be used to roughly estimate the average distance between the defects (L_{D}) that activate the D band [60]:

$$L_{\mathrm{D}}^2\,(\mathrm{nm}^2) = (1.8)\ \times\ 10^{-9}\,\lambda_{\mathrm{L}}^4\left(\frac{I_{\mathrm{D}}}{I_{\mathrm{G}}}\right)^{-1}, \tag{2}$$

where λ_{L} is the laser wavelength (in nm). Although equation 2 was obtained for vacancies (based on experiments on graphene irradiated with Ar ions with an energy of 90 eV), it is expected to be valid for other types of point defects as stated in reference [60], at least in the regime of large L_{D} taken here, where the nature of the defect is not expected to strongly affect the $I_{\mathrm{D}}/I_{\mathrm{G}}$ ratio. One can therefore expect this equation to provide at least a rough estimation of L_{D} in our samples, which were implanted at energies below the threshold for vacancy formation, *i.e.*, where bond disorder is therefore the dominant type of defect. Indeed, a comparable evolution of the $I_{\mathrm{D}}/I_{\mathrm{G}}$ ratio was observed for graphene irradiated with 5–20 keV electrons [62], *i.e.*, also well below the threshold for vacancy formation. In the context of the present work, where it is instructive to compare the observed disorder with the number of ions that produce it (*i.e.*, the fluence), we can convert this equation into an estimation of the defect areal concentration, that is, L_{D}^{-2}, given by:

$$\frac{1}{L_{\mathrm{D}}^2}\,(\mathrm{cm}^{-2}) = (5.5)\ \times\ 10^{22}\,\lambda_{\mathrm{L}}^{-4}\left(\frac{I_{\mathrm{D}}}{I_{\mathrm{G}}}\right). \tag{3}$$

These values are plotted in figure 9c. Since equation 2 is only valid when $\mathrm{L_D} \geq$ 10 nm [60] (which is within *stage 1* since the transition into *stage 2* happens when

L_D = 3 nm), equation 3 is valid only when the defect concentration is of the order or below 10^{12} cm^{-2}. We highlight this validity region (grey box) in figure 9c. Outside the grey box the disorder concentration is expected to deviate from equation 2 [60]. Up to the validity limit (25 eV for Ne and 30 eV for He), we reach a concentration of $\sim 1\times10^{12}$/cm^2; comparing to the implantation fluence of 10^{15} atoms/cm^2, this indicates that approximately ∼ 1000 impinging ions are necessary to produce a single observable defect. Although a crude estimate, this small ion-to-defect ratio indicates that isolated bond defects are metastable, likely experiencing dynamic annealing and agglomeration, as also suggested above for Gr/Pt. This notion of higher stability for defect agglomerates compared to more isolated defects is further supported by the observed fluence-dependence, presented next.

3.2.4. Disorder accumulation as a function of fluence. Figure 10 shows the Raman spectra of Gr/Cu implanted with He at 25 eV, as a function of implantation concentration (from 28% to 85%), which we define as the fluence (number of implanted ions per surface area) divided by the C surface density of graphene (number of C atoms per unit area). The *D* band versus *G* band ratios are plotted in figure 11. The other parameters extracted from the analysis are presented in figure S9 in the supplementary material. At low fluence (corresponding to a concentration of 28%) no *D* band is observed; at higher fluences, 56% and 85%, a *D* band emerges and steadily increases with fluence. The fact that the defect density (plotted in figure 11c, using equation 3) extrapolates to zero at a non-zero fluence (larger than 28%) suggests that there is a fluence threshold below which these defects are not created as efficiently or are efficiently annealed within a short time scale (dynamic annealing). Since the collision events of the impinging ions can be considered uncorrelated with respect to each other, the absence of measurable disorder at low fluence should not be a result of lower creation efficiency but instead of more efficient dynamic annealing. In other words, whereas for fluence values the (mostly isolated) defects that are created experience efficient dynamic annealing, the increase in fluence leads to defect agglomeration, and therefore higher stability, so that the accumulated disorder scales more strongly with implanted fluence. This picture of isolated bond defects being metastable, experiencing diffusion and self-assembly into more stable extended (*e.g.*, 1D-like) defects is also supported by (i) the defect agglomerates observed in the STM data and (ii) the overall low ratio of defect density to fluence (∼ 1/1000), that is, much lower than the simulated defect formation probabilities (of the order of unity, figure 5).

4. Discussion

Bond disorder has been observed or proposed in studies where graphene was irradiated with low-energy electrons (*i.e.*, where the transferred kinetic energy remains below E_t) [62, 63, 64] and photons of various wavelengths, for example, visible laser light [65, 66], extreme ultraviolet light [64, 67], and X-rays [68]. In reference [64],

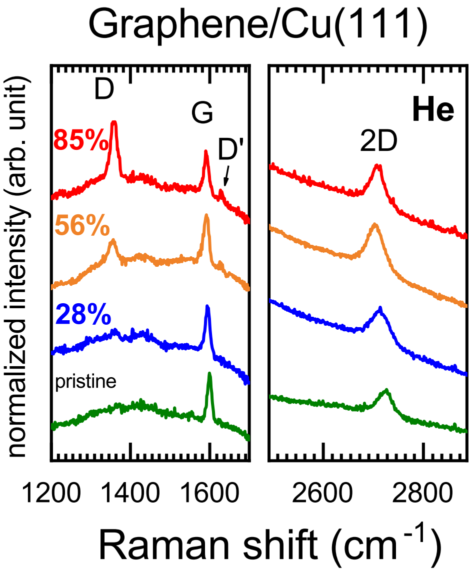

Figure 10. Raman spectra for He implanted Gr/Cu, as a function of He fluence corresponding to 28%, 56% and 85% of the surface density of C in a Gr/Cu layer.

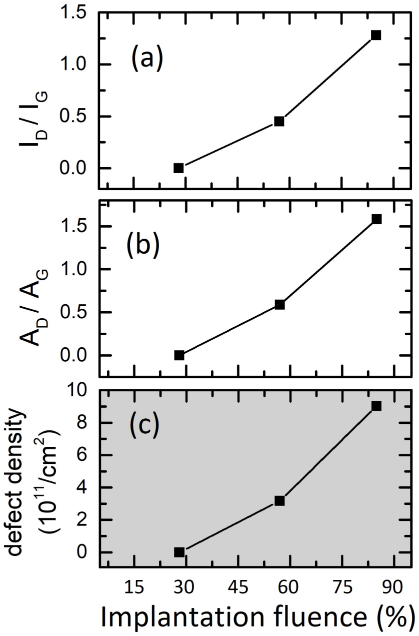

Figure 11. *D versus G* ratio of intensity (a) and integrated area (b), for He implanted Gr/Cu, as a function of the He fluence corresponding to 28%, 56% and 85% of the surface density of C in a Gr/Cu layer. (c) $1/\mathrm{L}_\mathrm{D}^2$ (as an estimation of the defect concentration) calculated using equation 2. All three data points are within the grey area that marks the regime where equation 2 is valid, that is, in which the average distance between point defects (L_D) $\geq$ 10 nm.

defect formation in graphene was studied by comparing the effect of extreme ultraviolet radiation and low-energy electron beams (80 eV, *i.e.*, orders of magnitude lower than that required to produce vacancies, ≈ 80 keV [31, 69]). The Raman D band was found to evolve as a function of the electron-beam dose. The authors conclude that the photoelectron excitation is responsible for the breaking of sp^2 bonds and formation of sp^3 bonds. The evolution of the Raman D band follows the amorphization trajectory, where the graphene is gradually disassembled by the irradiation, that is, transformed into a network of graphene nanocrystallites, and eventually amorphized [49]. The self-assembly of the point defects into extended 1D defects that we report here can be understood as the mechanism responsible for this often proposed disassembly of graphene upon irradiation-induced bond breaking, that is, the decomposition of single-crystal graphene layers into interconnected nanocrystallites [62, 63, 64, 65, 66, 64, 67, 68]. The self-assembled 1D defects that we observe with STM are likely to constitute the initial phase of formation of the grain boundaries between these interconnected nanocrystallites in disassembled graphene, which typically have characteristic length scales of the order of 10 nm, just like the typical separation between the self assembled 1D bond defects revealed by our STM data (figure 4). While for these lighter particles (electrons and photons), given the negligible kinetic-energy transfer to the C nuclei, the bond breaking is likely induced purely by electronic excitation [70] and ionization, in the present case (ions) it is plausible that both kinetic-energy transfer and electronic excitation/ionization play a role. Future studies, combining MD simulations and density functional theory (DFT) calculations [71], may provide further insight into these effects.

Although this work has focused on the bond defects, it is important to note the effect of the presence of the substrate on the formation of vacancy defects. Comparing the MD results reported here (for graphene on Pt) with those reported in reference [11] (for free-standing graphene), using the same MD approach, there is a significant increase in the minimum ion energy required to form a stable vacancy. Taking Ne as implanted element, for which the onset of vacancy formation can be clearly identified in both cases, while for free-standing graphene the vacancy formation probability increases from 0 to 9% between 25 eV and 30 eV [11], for Gr/Pt the probability increases from 0 to 1% between 30 eV and 40 eV. This increase in threshold displacement energy E_t (of the order of 10 eV) can be easily understood as resulting from the presence of the substrate, that is, although the impinging ion is still able to transfer momentum to the C atom in the direction of the substrate (vacuum for free-standing graphene), this C atom is recoiled back in the direction of the graphene plane upon collision with the substrate atoms. Producing a stable vacancy therefore requires an additional amount of energy for the C atom to be sufficiently displaced from its original position in the graphene lattice, for example, being incorporated into the substrate subsurface. This is an important effect to consider when ULE ion implantation is used for substitutional doping of graphene, which requires formation of a vacancy that can be occupied by the implanted ion. In particular, it may explain the low efficiency for substitutional incorporation of 40 eV Mn [8]. Future experimental studies, supported by combined molecular dynamics and density functional theory [71] taking into account the presence of the substrate, and extending the range to higher energies, will allow to further optimize the process of substitutional doping and understand the underlying mechanisms.

While here we have focused on studying the formation of these bond defects, by characterizing as-implanted samples, our results raise important questions regarding the stability of these bond defects against thermal annealing, for example, towards further agglomeration, restoration of the sp^2 C-C bonds, etc. Similarly, it will be interesting to study the (local) electronic properties of these bond defects, for example, using scanning tunneling spectroscopy, as well as their effect on the electronic structure of graphene, for example, using angle resolved photoemission spectroscopy (ARPES). Finally, it will also be interesting to investigate the chemical activity of these bond defects in graphene, for example, in the context of catalysis and capture of pollutants. While the present results on Gr/Pt and Gr/Cu indicate that the dangling bonds formed upon ion irradiation are mostly passivated via bond formation with the substrate atoms, it is plausible that the use of more inert substrates would result in a significant fraction of dangling bonds remaining as chemically-active sites.

5. Conclusion

We studied the defect formation in graphene resulting from ultralow energy ion implantation. As model systems, we used graphene grown on Cu(111) and on Pt(111), subsequently implanted with He, Ne and Ar with energies between 15 eV and 40 eV, to a fluence of 1×10^{15} ions per cm^2. A combination of Raman spectroscopy, scanning tunneling microscopy and MD simulations revealed the formation of bond defects. Such a defect is formed when an impinging ion interacts (Coulomb collision) with one or more C atoms in the graphene layer. This interaction results in the breaking of C-C sp^2 bonds and formation of C-substrate bonds. These defects are formed down to ion energies of 15 eV, significantly below the energies required to form stable vacancies. The formation probability increases with increasing energy and atomic number of the impinging element. Moreover, our data strongly suggests that isolated bond defects are metastable at room temperature, being prone to dynamic annealing and agglomeration into more stable defect complexes. Similar bond disorder has been previously reported for graphene irradiated with photons and low-energy electrons. While for these lighter particles, the bond breaking is induced by electronic excitation/ionization, in the case reported here, for ions, the transfer of kinetic energy to the C atom during the collision is likely to also play an important role. In particular, the decrease in distance (during the collision) between the recoiled C atom and the substrate surface atoms may assist the formation of C-substrate bonds. Our Raman data indicate that the formation of these bond defects is accompanied by an increase in tensile strain in graphene, which can be understood as due to the local C-C bond stretching required to accommodate this deviation from flat graphene.

These findings significantly advance our understanding of disorder induced in graphene by ULE ion implantation, which is relevant in arguably any application context, such as electronic or chemical functionalization. In addition, they reveal new questions and application opportunities. On the one hand, they motivate further research towards a deeper understanding of these bond defects: their formation mechanism (*e.g.*, the roles of electronic excitation/ionization *versus* momentum transfer in a collision); their thermal stability (*e.g.*, with respect to diffusion, agglomeration and annealing); their local electronic properties and their effect on band structure of graphene. On the other hand, future research on the chemical activity of these bond defects in graphene may reveal exploitation possibilities, for example, in the context of catalysis and of covalent functionalization with molecular groups. The fact that this type of defects is created in the low energy limit (at least down to 15 eV), would allow to controllably generate them while avoiding the formation of other defects such as vacancies.

Declaration of competing interest

The authors declare that they have no known competing financial interests or personal relationships that could have appeared to influence the work reported in this paper.

Acknowledgements

This work was funded by KU Leuven and FWO Vlaanderen. E.H.Å acknowledges funding from Austrian Science Fund (FWF) project number M2595. The authors acknowledge Elettra Sincrotrone Trieste for providing access to its synchrotron radiation facilities and, in particular, to the SuperESCA beamline. The authors thank P. Lacovig and S. Lizzit for the support during the XPS beam time at SuperESCA, Elettra. The access to the Elettra Sincrotrone Trieste has been supported by the project CALIPSOplus under Grant Agreement 730872 from the EU Framework Programme for Research and Innovation HORIZON 2020.

Appendix A. Supplementary data

The supplementary data to this article consist of:

- Additional MD results
- Additional data for Gr/Pt with accompanying references [72, 73]
- Additional data for Gr/Cu with accompanying references [74, 75, 76, 77, 38, 78, 79, 80]

References

[1] U. Bangert, W. Pierce, D. Kepaptsoglou, Q. Ramasse, R. Zan, M. Gass, *et al.*, "Ion implantation of graphene - toward ic compatible technologies," *Nano Letters*, vol. 13, no. 10, pp. 4902–4907, 2013.

[2] P. Willke, J. Amani, S. Thakur, S. Weikert, T. Druga, K. Maiti, *et al.*, "Short-range ordering of ion-implanted nitrogen atoms in sic-graphene," *Applied Physics Letters*, vol. 105, no. 11, p. 111605, 2014.

[3] D. Kepaptsoglou, T. P. Hardcastle, C. R. Seabourne, U. Bangert, R. Zan, J. A. Amani, *et al.*, "Electronic structure modification of ion implanted graphene: The spectroscopic signatures of p- and n-type doping," *ACS Nano*, vol. 9, no. 11, pp. 11398–11407, 2015.

[4] P. Willke, J. A. Amani, A. Sinterhauf, S. Thakur, T. Kotzott, T. Druga, *et al.*, "Doping of graphene by low-energy ion beam implantation: structural, electronic, and transport properties," *Nano Letters*, vol. 15, no. 8, pp. 5110–5115, 2015.

[5] C. D. Cress, S. W. Schmucker, A. L. Friedman, P. Dev, J. C. Culbertson, J. W. Lyding, *et al.*, "Nitrogen-doped graphene and twisted bilayer graphene *via* hyperthermal ion implantation with depth control," *ACS Nano*, vol. 10, no. 3, pp. 3714–3722, 2016.

[6] T. Susi, T. P. Hardcastle, H. Hofsäss, A. Mittelberger, T. J. Pennycook, C. Mangler, *et al.*, "Single-atom spectroscopy of phosphorus dopants implanted into graphene," *2D Materials*, vol. 4, no. 2, p. 021013, 2017.

[7] M. Tripathi, A. Markevich, R. Bottger, S. Facsko, E. Besley, J. Kotakoski, *et al.*, "Implanting germanium into graphene," *ACS Nano*, vol. 12, no. 5, pp. 4641–4647, 2018.

[8] P.-C. Lin, R. Villarreal, S. Achilli, H. Bana, M. N. Nair, A. Tejeda, *et al.*, "Doping graphene with substitutional mn," *ACS Nano*, vol. 15, no. 3, pp. 5449–5458, 2021.

[9] P.-C. Lin, R. Villarreal, H. Bana, Z. Zarkua, V. Hendriks, H.-C. Tsai, *et al.*, "Thermal annealing of graphene implanted with mn at ultralow energies: From disordered and contaminated to nearly pristine graphene," *The Journal of Physical Chemistry C*, vol. 126, no. 25, pp. 10494–10505, 2022.

[10] A. Trentino, K. Mizohata, G. Zagler, M. Längle, K. Mustonen, T. Susi, *et al.*, "Two-step implantation of gold into graphene," *2D Materials*, vol. 9, no. 2, p. 025011, 2022.

[11] R. Villarreal, P.-C. Lin, F. Faraji, N. Hassani, H. Bana, Z. Zarkua, *et al.*, "Breakdown of universal scaling for nanometer-sized bubbles in graphene," *Nano Letters*, vol. 21, no. 19, p. 8103–8110, 2021.

[12] F. Banhart, J. Kotakoski, and A. V. Krasheninnikov, "Structural defects in graphene," *ACS Nano*, vol. 5, no. 1, pp. 26–41, 2011.

[13] D. Boukhvalov and M. Katsnelson, "Chemical functionalization of graphene with defects," *Nano letters*, vol. 8, no. 12, pp. 4373–4379, 2008.

[14] Y. Wei, J. Wu, H. Yin, X. Shi, R. Yang, and M. Dresselhaus, "The nature of strength enhancement and weakening by pentagon–heptagon defects in graphene," *Nature materials*, vol. 11, no. 9, pp. 759–763, 2012.

[15] R. Nair, M. Sepioni, I.-L. Tsai, O. Lehtinen, J. Keinonen, A. Krasheninnikov, *et al.*, "Spin-half paramagnetism in graphene induced by point defects," *Nature Physics*, vol. 8, no. 3, pp. 199–202, 2012.

[16] V. Tozzini and V. Pellegrini, "Reversible hydrogen storage by controlled buckling of graphene layers," *The Journal of Physical Chemistry C*, vol. 115, no. 51, pp. 25523–25528, 2011.

[17] J. Guo, J. R. Morris, Y. Ihm, C. I. Contescu, N. C. Gallego, G. Duscher, *et al.*, "Topological defects: origin of nanopores and enhanced adsorption performance in nanoporous carbon," *small*, vol. 8, no. 21, pp. 3283–3288, 2012.

[18] Y. Ito, Y. Shen, D. Hojo, Y. Itagaki, T. Fujita, L. Chen, *et al.*, "Correlation between chemical dopants and topological defects in catalytically active nanoporous graphene," *Advanced Materials*, vol. 28, no. 48, pp. 10644–10651, 2016.

[19] J. Wang, B. Chen, and B. Xing, "Wrinkles and folds of activated graphene nanosheets as fast and efficient adsorptive sites for hydrophobic organic contaminants," *Environmental science & technology*, vol. 50, no. 7, pp. 3798–3808, 2016.

[20] J. Wang, Z. Chen, and B. Chen, "Adsorption of polycyclic aromatic hydrocarbons by graphene and graphene oxide nanosheets," *Environmental science & technology*, vol. 48, no. 9, pp. 4817–4825,

2014.

[21] O. Glukhova and M. Slepchenkov, "Influence of the curvature of deformed graphene nanoribbons on their electronic and adsorptive properties: theoretical investigation based on the analysis of the local stress field for an atomic grid," *Nanoscale*, vol. 4, no. 11, pp. 3335–3344, 2012.

[22] D. W. Boukhvalov and M. I. Katsnelson, "Enhancement of chemical activity in corrugated graphene," *The Journal of Physical Chemistry C*, vol. 113, no. 32, pp. 14176–14178, 2009.

[23] F. L. Thiemann, P. Rowe, A. Zen, E. A. Muller, and A. Michaelides, "Defect-dependent corrugation in graphene," *Nano Letters*, vol. 21, no. 19, pp. 8143–8150, 2021.

[24] M. M. Lucchese, F. Stavale, E. M. Ferreira, C. Vilani, M. V. d. O. Moutinho, R. B. Capaz, *et al.*, "Quantifying ion-induced defects and raman relaxation length in graphene," *Carbon*, vol. 48, no. 5, pp. 1592–1597, 2010.

[25] O. Lehtinen, J. Kotakoski, A. Krasheninnikov, A. Tolvanen, K. Nordlund, and J. Keinonen, "Effects of ion bombardment on a two-dimensional target: Atomistic simulations of graphene irradiation," *Physical Review B*, vol. 81, no. 15, p. 153401, 2010.

[26] G. Zamborlini, M. Imam, L. L. Patera, T. O. Mentes, N. Stojic, C. Africh, *et al.*, "Nanobubbles at gpa pressure under graphene," *Nano Letters*, vol. 15, no. 9, pp. 6162–6169, 2015.

[27] H. Cun, M. Iannuzzi, A. Hemmi, J. Osterwalder, and T. Greber, "Ar implantation beneath graphene on ru(0001): Nanotents and "can-opener" effect," *Surface Science*, vol. 634, pp. 95–102, 2015.

[28] C. Herbig, E. H. Åhlgren, U. A. Schröder, A. J. Martinez-Galera, M. A. Arman, J. Kotakoski, *et al.*, "Xe irradiation of graphene on ir(111): from trapping to blistering," *Physical Review B*, vol. 92, no. 8, p. 085429, 2015.

[29] E. H. Åhlgren, S. Hämäläinen, O. Lehtinen, P. Liljeroth, and J. Kotakoski, "Structural manipulation of the graphene/metal interface with ar+ irradiation," *Physical Review B*, vol. 88, no. 15, p. 155419, 2013.

[30] J. Kotakoski, C. H. Jin, O. Lehtinen, K. Suenaga, and A. V. Krasheninnikov, "Electron knock-on damage in hexagonal boron nitride monolayers," *Physical Review B*, vol. 82, no. 11, p. 113404, 2010.

[31] J. C. Meyer, F. Eder, S. Kurasch, V. Skakalova, J. Kotakoski, H. J. Park, *et al.*, "Accurate measurement of electron beam induced displacement cross sections for single-layer graphene," *Physical Review Letters*, vol. 108, no. 19, p. 196102, 2012.

[32] P. Ahlberg, F. Johansson, Z.-B. Zhang, U. Jansson, S.-L. Zhang, A. Lindblad, *et al.*, "Defect formation in graphene during low-energy ion bombardment," *APL Materials*, vol. 4, no. 4, p. 046104, 2016.

[33] S. Kretschmer, S. Ghaderzadeh, S. Facsko, and A. V. Krasheninnikov, "Threshold ion energies for creating defects in 2d materials from first-principles calculations: Chemical interactions are important," *The Journal of Physical Chemistry Letters*, vol. 13, pp. 514–519, 2022.

[34] K. Verguts, Y. Defossez, A. Leonhardt, J. De Messemaeker, K. Schouteden, C. Van Haesendonck, *et al.*, "Growth of millimeter-sized graphene single crystals on al_2o_3(0001)/pt(111) template wafers using chemical vapor deposition," *ECS Journal of Solid State Science and Technology*, vol. 7, no. 12, 2018. M195.

[35] K. Verguts, N. Vrancken, B. Vermeulen, C. Huyghebaert, H. Terryn, S. Brems, *et al.*, "Single-layer graphene synthesis on a al_2o_3(0001)/cu(111) template using chemical vapor deposition," *ECS Journal of Solid State Science and Technology*, vol. 5, no. 11, 2016. Q3060.

[36] Z. Li, S. Li, H.-Y. T. Chen, N. Gao, K. Schouteden, X. Qiang, J. Zhao, S. Brems, C. Huyghebaert, and C. Van Haesendonck, "Strongly hole-doped and highly decoupled graphene on platinum by water intercalation," *The Journal of Physical Chemistry Letters*, vol. 10, no. 14, pp. 3998–4002, 2019.

[37] K. Verguts, K. Schouteden, C.-H. Wu, L. Peters, N. Vrancken, X. Wu, Z. Li, M. Erkens, C. Porret, C. Huyghebaert, *et al.*, "Controlling water intercalation is key to a direct graphene transfer," *ACS Applied Materials & Interfaces*, vol. 9, no. 42, pp. 37484–37492, 2017.

[38] R. Blume, P. R. Kidambi, B. C. Bayer, R. S. Weatherup, Z.-J. Wang, G. Weinberg, *et al.*, "The influence of intercalated oxygen on the properties of graphene on polycrystalline cu under various environmental conditions," *Physical Chemistry Chemical Physics*, vol. 16, no. 47, pp. 25989–26003, 2014.

[39] M. Auge, F. Junge, and H. Hofsäss, "Laterally controlled ultra-low energy ion implantation using electrostatic masking," *Nuclear Instruments and Methods in Physics Research Section B: Beam Interactions with Materials and Atoms*, vol. 512, pp. 96–101, 2022.

[40] K. Albe, K. Nordlund, and R. S. Averback, "Modeling the metal-semiconductor interaction: Analytical bond-order potential for platinum-carbon," *Physical Review B*, vol. 65, p. 195124, 2002.

[41] D. W. Brenner, O. A. Shenderova, J. A. Harrison, S. J. Stuart, B. Ni, and S. B. Sinnott, "A second-generation reactive empirical bond order (rebo) potential energy expression for hydrocarbons," *Journal of Physics: Condensed Matter*, vol. 14, no. 4, pp. 783–802, 2002.

[42] J. Ziegler and J. Biersack, *The stopping and range of ions in matter*, pp. 93–129. Springer, 1985.

[43] H. J. Berendsen, J. v. Postma, W. F. van Gunsteren, A. DiNola, and J. R. Haak, "Molecular dynamics with coupling to an external bath," *The Journal of Chemical Physics*, vol. 81, no. 8, pp. 3684–3690, 1984.

[44] Q. Zhou, S. Coh, M. L. Cohen, S. G. Louie, and A. Zettl, "Imprint of transition metal d orbitals on a graphene dirac cone," *Physical Review B*, vol. 88, no. 23, p. 235431, 2013.

[45] T. L. Alford, L. C. Feldman, and J. W. Mayer, *Atomic collisions and backscattering spectrometry*, pp. 12–33. Springer US, 2007.

[46] H. W. Kim, J. Ku, W. Ko, Y. Cho, I. Jeon, and S. W. Hwang, "Quenching of the resonant states of single carbon vacancies in graphene/pt (111)," *The Journal of Physical Chemistry C*, vol. 121, no. 44, pp. 24641–24647, 2017.

[47] S. Li, M. Liu, and X. Qiu, "Scanning probe microscopy of topological structure induced electronic states of graphene," *Small Methods*, vol. 4, no. 3, p. 1900683, 2020.

[48] N. Blanc, F. Jean, A. V. Krasheninnikov, G. Renaud, and J. Coraux, "Strains induced by point defects in graphene on a metal," *Physical Review Letters*, vol. 111, no. 8, p. 085501, 2013.

[49] A. C. Ferrari, "Raman spectroscopy of graphene and graphite: Disorder, electron–phonon coupling, doping and nonadiabatic effects," *Solid state communications*, vol. 143, no. 1-2, pp. 47–57, 2007.

[50] A. Jorio, M. M. Lucchese, F. Stavale, E. H. M. Ferreira, M. V. Moutinho, R. B. Capaz, *et al.*, "Raman study of ion-induced defects in n-layer graphene," *Journal of Physics: Condensed Matter*, vol. 22, no. 33, p. 334204, 2010.

[51] J. Ribeiro-Soares, M. Oliveros, C. Garin, M. David, L. Martins, C. Almeida, *et al.*, "Structural analysis of polycrystalline graphene systems by raman spectroscopy," *Carbon*, vol. 95, pp. 646–652, 2015.

[52] A. Eckmann, A. Felten, A. Mishchenko, L. Britnell, R. Krupke, K. S. Novoselov, *et al.*, "Probing the nature of defects in graphene by raman spectroscopy," *Nano Letters*, vol. 12, no. 8, pp. 3925–3930, 2012.

[53] A. Das, S. Pisana, B. Chakraborty, S. Piscanec, S. K. Saha, U. V. Waghmare, *et al.*, "Monitoring dopants by raman scattering in an electrochemically top-gated graphene transistor," *Nature Nanotechnology*, vol. 3, no. 4, pp. 210–215, 2008.

[54] H. Sojoudi, J. Baltazar, C. Henderson, and S. Graham, "Impact of post-growth thermal annealing and environmental exposure on the unintentional doping of cvd graphene films," *Journal of Vacuum Science & Technology B, Nanotechnology and Microelectronics: Materials, Processing, Measurement, and Phenomena*, vol. 30, no. 4, p. 041213, 2012.

[55] J. Zabel, R. R. Nair, A. Ott, T. Georgiou, A. K. Geim, K. S. Novoselov, *et al.*, "Raman spectroscopy of graphene and bilayer under biaxial strain: bubbles and balloons," *Nano Letters*, vol. 12, no. 2, pp. 617–621, 2012.

[56] J. Choi, S. Koo, M. Song, D. Y. Jung, S.-Y. Choi, and S. Ryu, "Varying electronic coupling at graphene–copper interfaces probed with raman spectroscopy," *2D Materials*, vol. 7, no. 2,

p. 025006, 2020.

[57] R. Wu, L. Gan, X. Ou, Q. Zhang, and Z. Luo, "Detaching graphene from copper substrate by oxidation-assisted water intercalation," *Carbon*, vol. 98, pp. 138–143, 2016.

[58] X. Yin, Y. Li, F. Ke, C. Lin, H. Zhao, L. Gan, *et al.*, "Evolution of the raman spectrum of graphene grown on copper upon oxidation of the substrate," *Nano Research*, vol. 7, no. 11, pp. 1613–1622, 2014.

[59] R. Saito, M. Hofmann, G. Dresselhaus, A. Jorio, and M. Dresselhaus, "Raman spectroscopy of graphene and carbon nanotubes," *Advances in Physics*, vol. 60, no. 3, pp. 413–550, 2011.

[60] L. G. Cançado, A. Jorio, E. M. Ferreira, F. Stavale, C. A. Achete, R. B. Capaz, *et al.*, "Quantifying defects in graphene via raman spectroscopy at different excitation energies," *Nano Letters*, vol. 11, no. 8, pp. 3190–3196, 2011.

[61] A. Eckmann, A. Felten, I. Verzhbitskiy, R. Davey, and C. Casiraghi, "Raman study on defective graphene: Effect of the excitation energy, type, and amount of defects," *Physical Review B*, vol. 88, no. 3, p. 035426, 2013.

[62] D. Teweldebrhan and A. A. Balandin, "Modification of graphene properties due to electron-beam irradiation," *Applied Physics Letters*, vol. 94, no. 1, p. 013101, 2009.

[63] M. Iqbal, A. Kumar Singh, M. Iqbal, S. Seo, and J. Eom, "Effect of e-beam irradiation on graphene layer grown by chemical vapor deposition," *Journal of Applied Physics*, vol. 111, no. 8, p. 084307, 2012.

[64] A. Gao, C. J. Lee, and F. Bijkerk, "Graphene defect formation by extreme ultraviolet generated photoelectrons," *Journal of Applied Physics*, vol. 116, no. 5, p. 054312, 2014.

[65] B. Krauss, T. Lohmann, D.-H. Chae, M. Haluska, K. von Klitzing, and J. H. Smet, "Laser-induced disassembly of a graphene single crystal into a nanocrystalline network," *Physical Review B*, vol. 79, no. 16, p. 165428, 2009.

[66] Y. Stubrov, A. Nikolenko, V. Strelchuk, S. Nedilko, and V. Chornii, "Structural modification of single-layer graphene under laser irradiation featured by micro-raman spectroscopy," *Nanoscale research letters*, vol. 12, no. 1, pp. 1–6, 2017.

[67] S. Botti, L. Mezi, A. Rufoloni, A. Vannozzi, S. Bollanti, and F. Flora, "Extreme ultraviolet generation of localized defects in single-layer graphene: Raman mapping, atomic force microscopy, and high-resolution scanning electron microscopy analysis," *ACS Applied Electronic Materials*, vol. 1, no. 12, pp. 2560–2565, 2019.

[68] S. Zhou, Ç. Girit, A. Scholl, C. Jozwiak, D. Siegel, P. Yu, *et al.*, "Instability of two-dimensional graphene: Breaking sp^2 bonds with soft x rays," *Physical Review B*, vol. 80, no. 12, p. 121409, 2009.

[69] T. Susi, J. C. Meyer, and J. Kotakoski, "Quantifying transmission electron microscopy irradiation effects using two-dimensional materials," *Nature Reviews Physics*, vol. 1, no. 6, pp. 397–405, 2019.

[70] N. Medvedev, H. Noei, S. Toleikis, and B. Ziaja, "Response of free-standing graphene monolayer exposed to ultrashort intense xuv pulse from free-electron laser," *The Journal of Chemical Physics*, vol. 154, no. 20, p. 204706, 2021.

[71] E. H. Åhlgren, J. Kotakoski, and A. Krasheninnikov, "Atomistic simulations of the implantation of low-energy boron and nitrogen ions into graphene," *Physical Review B*, vol. 83, no. 11, p. 115424, 2011.

[72] Z. Zhu, F. Tao, F. Zheng, R. Chang, Y. Li, L. Heinke, *et al.*, "Formation of nanometer-sized surface platinum oxide clusters on a stepped pt (557) single crystal surface induced by oxygen: a high-pressure stm and ambient-pressure xps study," *Nano letters*, vol. 12, no. 3, pp. 1491–1497, 2012.

[73] R. Arrigo, M. Hävecker, M. E. Schuster, C. Ranjan, E. Stotz, A. Knop-Gericke, *et al.*, "In situ study of the gas-phase electrolysis of water on platinum by nap-xps," *Angewandte Chemie International Edition*, vol. 52, no. 44, pp. 11660–11664, 2013.

[74] M. Bruna, A. K. Ott, M. Ijass, D. Yoon, U. Sassi, and A. C. Ferrari, "Doping dependence of the

raman spectrum of defected graphene," *ACS Nano*, vol. 8, no. 7, pp. 7432–7441, 2014.

[75] B. Deng, Z. Pang, S. Chen, X. Li, C. Meng, J. Li, *et al.*, "Wrinkle-free single-crystal graphene wafer grown on strain-engineered substrates," *ACS Nano*, vol. 11, no. 12, pp. 12337–12345, 2017.

[76] J. Kwak, Y. Jo, S.-D. Park, N. Y. Kim, S.-Y. Kim, H.-J. Shin, *et al.*, "Oxidation behavior of graphene-coated copper at intrinsic graphene defects of different origins," *Nature Communications*, vol. 8, no. 1, p. 1549, 2017.

[77] J. Yeh and I. Lindau, "Atomic subshell photoionization cross sections and asymmetry parameters," *Atomic Data and Nuclear Data Tables*, vol. 32, no. 1, pp. 1–155, 1985.

[78] M. Scardamaglia, C. Struzzi, A. Zakharov, N. Reckinger, P. Zeller, M. Amati, *et al.*, "Highlighting the dynamics of graphene protection toward the oxidation of copper under operando conditions," *ACS Applied Materials & Interfaces*, vol. 11, no. 32, pp. 29448–29457, 2019.

[79] S. Poulston, P. Parlett, P. Stone, and M. Bowker, "Surface oxidation and reduction of cuo and cu_2o studied using xps and xaes," *Surface and Interface Analysis*, vol. 24, no. 12, pp. 811–820, 1996.

[80] K. Verguts, B. Vermeulen, N. Vrancken, K. Schouteden, C. V. Haesendonck, C. Huyghebaert, M. Heyns, S. D. Gendt, and S. Brems, "Epitaxial al_2o_3(0001)/cu(111) template development for cvd graphene growth," *The Journal of Physical Chemistry C*, vol. 120, no. 1, p. 297–304, 2016.

Bond defects created in graphene by ultralow energy ion implantation

1. Additional MD results

Figure S1 shows the probability of an impinging atom creating n C-Pt bonds, with n between 1 and 6. For a given element, with increasing energy, the distribution in n becomes broader and centered at higher values of n. For a given energy, a similar evolution is observed with increasing atomic number of the impinging element.

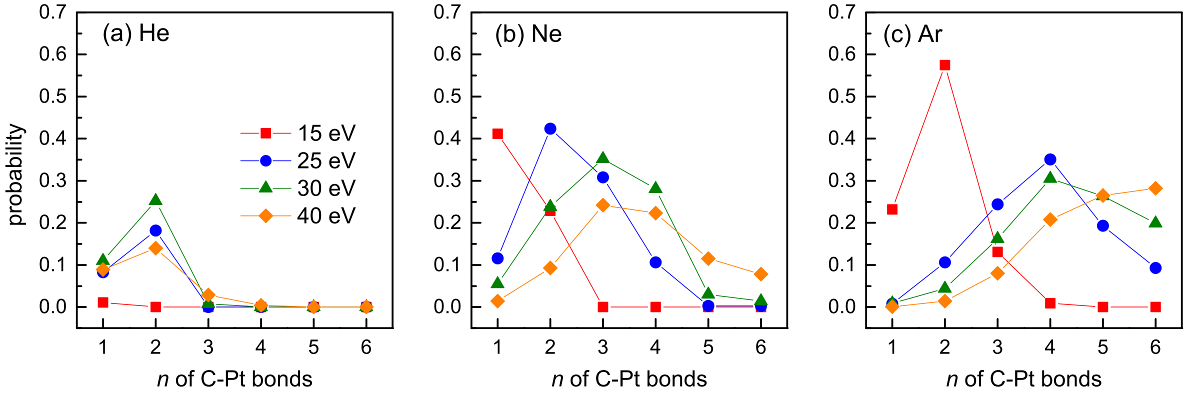

Figure S1. Probability (obtained from the MD simulations) of an impinging atom creating n C-Pt bonds, for energies between 15 eV and 40 eV, for the three noble gas elements: (a) He, (b) Ne, (c) Ar.

2. Additional data for Gr/Pt

2.1. Synchrotron XPS data for Gr/Pt

Figure S2 shows synchrotron XPS data on pristine Gr/Pt as well as Ne and Ar implanted Gr/Pt. The pristine sample exhibits, in addition to the graphitic C component (C in the graphene lattice), non-graphitic C components (81.40% with respect to the graphitic C) that are likely related to hydrocarbon contaminants and possibly some defects (*e.g.*, grain boundaries). A significant O signal is also observed (43.2% with respect to graphitic C), likely also related to the hydrocarbon components observed in the C core-level. The Pt signal is consistent with pure metallic Pt [72]. In the Ne implanted sample, we observe an increase in the non-graphitic C components (to 117.3%), which is likely related to an increase in defect-related components as well as hydrocarbon contaminants. An increase in the O signal (to 95.7%) is also observed, consistent with

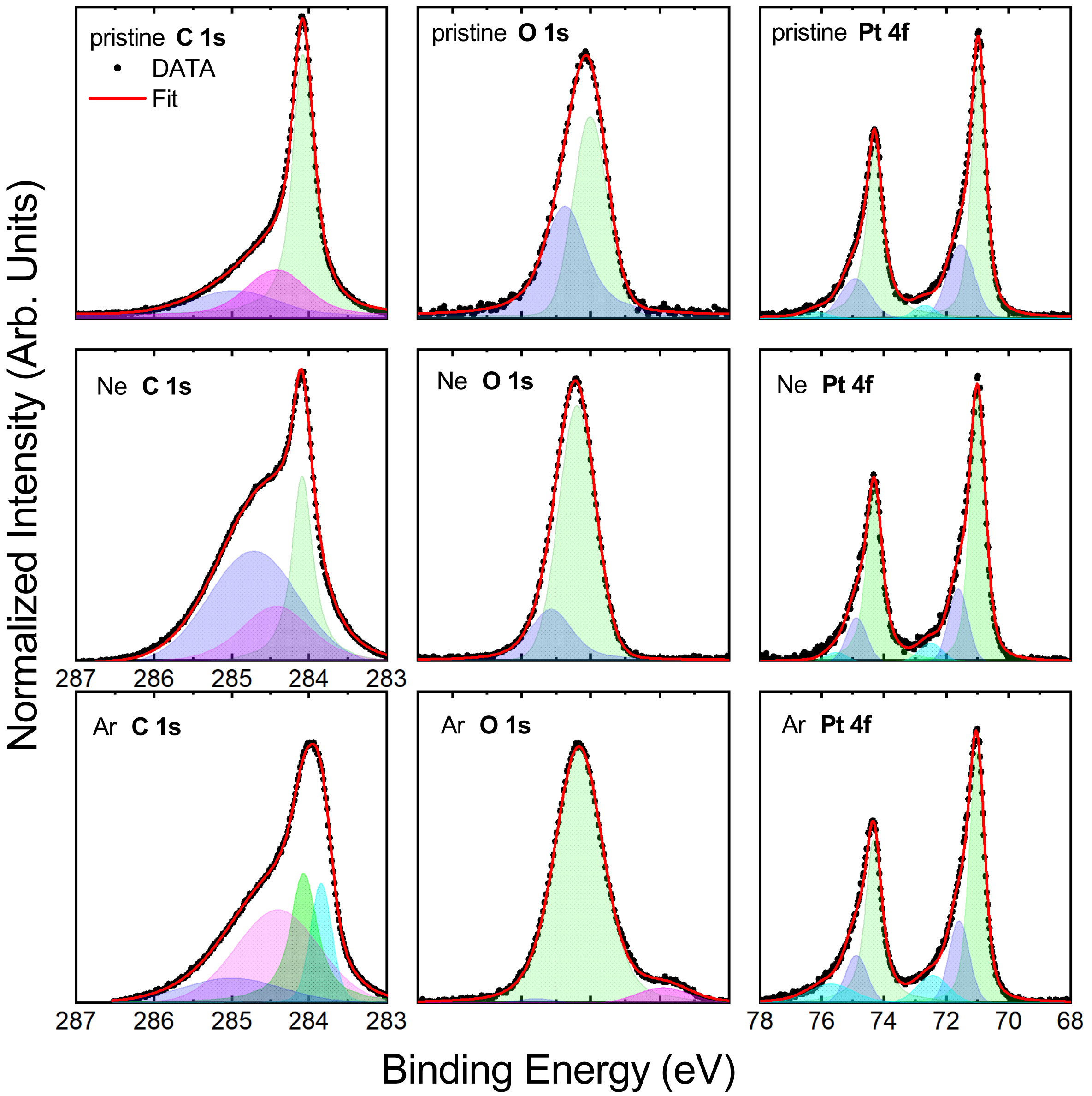

Figure S2. Synchrotron XPS spectra and fit for Gr/Pt(111), pristine (top) and implanted with 25 eV Ne (middle) and Ar (bottom) ions: (left) C 1s core-level, (center) O 1s core level, (right) Pt 4f core level.

an increase in hydrocarbon coverage. The Pt peak area decreases by 22% (compared to pristine sample), likely resulting from the increase in adsorbed hydrocarbons (*i.e.*, Pt is effectively deeper in this sample). In the Ar implanted sample, the C core-level becomes even more complex, that is, the ideal graphitic component appears to be replaced by a broader feature which we fit with two components. This effect is likely related to the even higher degree of disorder for Ar *versus* Ne implantation. The O signal also increases (to 111%), in particular, with the appearance of an additional component likely related to Pt-O and hydroxyl groups [73]. In the Pt signal a corresponding new component emerges related to hydrated Pt and O on Pt as 2D clusters [73]. This data

(C, O, Pt) on the Ar implanted sample suggests that the disorder increased to a level that it enhances water intercalation and oxidation.

In short, we see signs of increased disorder and hydrocarbon contamination induced by the implantation. Since the XPS measurements are performed *ex-situ*, it is likely that the additional C and O is adsorbed upon the short exposure to ambient, between the implantation and the XPS measurement, as the induced defects increase the reactivity of the graphene surface. However we do not observe a clear correlation between the amount of disorder and the amount of contamination. This lack of clear correlation is also observed for Gr/Cu (cf. section 3.3).

2.2. STM contrast of bond defects

We suspect that the emergence of a clear STM contrast associated with the bond defects requires a particular orbital symmetry of the last atom(s) at the tip apex or the tip to be functionalized (*e.g.*, by a hydrocarbon molecule picked up by the tip during the scan) as this contrast is not always observed regardless of whether the tip is atomically sharp or not. This may be related to a different orbital overlap between this last atom(s) at the tip apex with the C/Pt bond defect. In fact, we often see the contrast vary from one tip to the other during the scan. An example is presented in figure S3 for Ne implanted Gr/Pt, where the tip spontaneously changed around the middle of the scan. Here, while the Ne bubbles look equally sharp and the corrugation due to the lattice can be identified on both regions (functionalized tip and non functionalized tip), the contrast associated with the bond defects changes from sharp features to broader corrugations in the bottom half region of the scan (non functionalized tip region). This is consistent with the scenario that we propose in the main text: the defect feature observed in the STM micrographs (protrusions) are due to a change in LDOS resulting from C-Pt bonds that involve the C π-orbital rather than the σ-orbitals, as has been described for for C-Pt bonds in the neighborhood of single carbon vacancies in graphene/Pt [46, 47]. In such a scenario, one would indeed expect that functionalization of the tip would drastically change the orbital overlap between the π-orbital of the C atom(s) involved in the C-Pt bond and the orbitals of the atom at the tip apex, and thus the sensitivity to the LDOS associated with the bond defect.

3. Additional data for Gr/Cu

3.1. STM characterization of He and Ne implanted Gr/Cu

In figure S4, we compare the surface of pristine graphene to He and Ne implanted graphene. In the case of pristine graphene, we see the moiré superstructure resulting from the interference between the lattices of graphene and Cu(111) and some point-like depressions (indicated by black arrows) which are related to intercalated defects [8]. For the He implanted graphene, no additional features are observed. We note that the apparently increased amount of intercalated defects in the implanted sample (panel b)

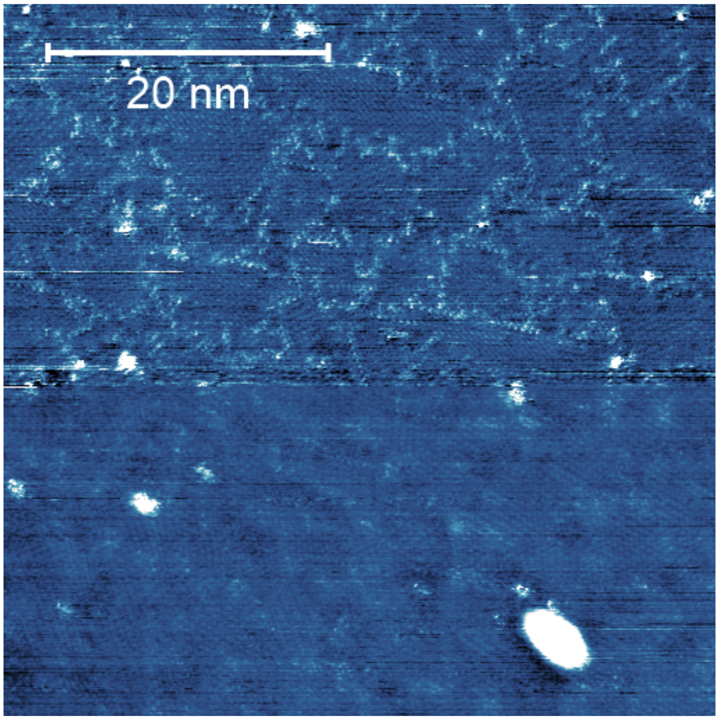

Figure S3. STM micrograph showing as-implanted 25 eV Ne Gr/Pt (measured at RT with V_{sample} = 50 mV, $I_{tun.}$ = 300 pA).

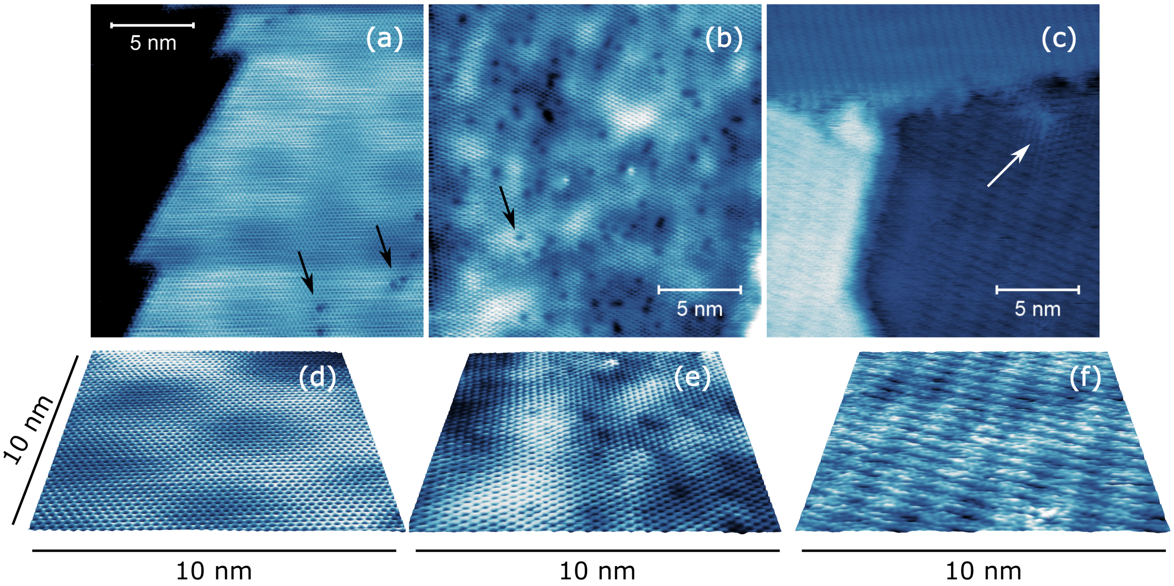

Figure S4. STM micrographs showing: (a,d) The moiré periodicity in pristine Gr/Cu (measured at RT with V_{sample} = -300 mV, $I_{tun.}$ = 100 pA); (b,e) As-implanted 25 eV He Gr/Cu (measured at 5 K with V_{sample} = -500 mV, $I_{tun.}$ = 50 pA) (c,f) As-implanted 25 eV Ne Gr/Cu (measured at RT with V_{sample} = -200 mV, $I_{tun.}$ = 200 pA).

is not representative; these intercalated defects are also present in the pristine surface and their density varies across the sample surface; this increase from panel (a) to panel

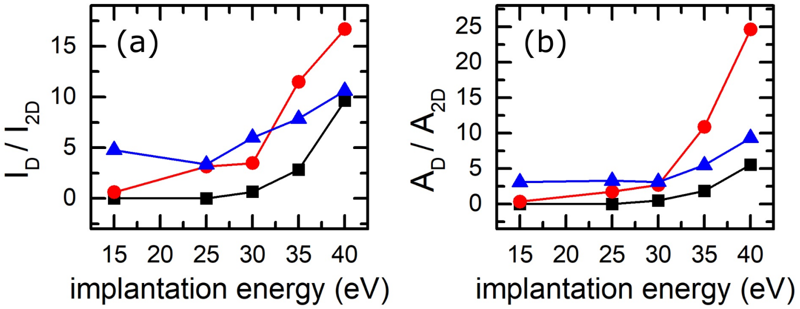

Figure S5. *D versus 2D* ratios, as a function of implantation energy (from 15 eV up to 40 eV), for the three implanted elements (He, Ne, Ar): (a) Intensity ratios; (b) Integrated area ratios. The standard deviation of the intensity ratio is ∼ ± 0.2; the standard deviation of the integrated ratio is ∼ ± 0.2 (determined by measuring multiple spots on the samples).

(b) is only apparent, and thus not related to the implantation. For the Ne implanted graphene, despite the multiple tip effect artefact in the micrograph; we are able to resolve a surface defect on the top left corner (indicated by a white arrow) and no additional features are observed in the surface. As discussed in the main text, although the Raman spectroscopy data show that bond defects are present both in Gr/Pt and Gr/Cu, we do not observe in Gr/Cu the characteristic perturbations of the LDOS that appear in the in STM micrographs of Gr/Pt (regardless of the tunneling parameters used), at least for these two cases of He and Ne implanted graphene at 25 eV. More thorough STM experiments will be necessary to understand why these perturbations to the LDOS are less clear in Gr/Cu, but one may relate their absence to the different interaction between graphene and Pt(111) compared to Cu(111). As described in the main text and in section 2.2 of the supplementary information, even for Gr/Pt the STM observation seems to depend on accidental tip functionalization and a specific overlap between tip orbitals and the π-orbital of the C atom involved in the bond defect. The fact that the bond disorder is not clearly observed in the STM data for Gr/Cu may simply result from the fact that the same conditions are not provided by the the C-Cu bonds in the Gr/Cu system. We also stress (as mentioned in section 3.1) that strong instabilities in the tunneling junction due to disorder and surface contamination make STM imaging of the as-implanted graphene challenging. Moreover, as shown in reference [80], as-grown graphene on Cu(111), which is then exposed to ambient conditions, tends to exhibit a high density of Cu steps and an annealing treatment is necessary; thus limiting the experimental conditions in which this thorough STM characterization could be done.

3.2. D *band versus* 2D *band ratio*

Although, as mentioned above, the $I_\mathrm{D}/I_\mathrm{G}$ ratio provides the most reliable insight into disorder formation in graphene, in the following we discuss the *2D* band for completeness. The intensity of the *2D* (G') band decreases monotonically as a function

Table S1. Oxygen to carbon (O/C) ratio for pristine and implanted Gr/Cu (25 eV), estimated from the C 1s and O 1s core-level peaks. The estimation is achieved by taking the integrated area and photoionization cross section into consideration, assuming the Cu(111) substrate is free of C and O (*i.e.*, all the observed C and O are in the vicinity of graphene). Photoionization cross section of C 1s and O 1s peak are 0.02228 and 0.06354 [77], respectively.

pristine	He implanted	Ne implanted	Ar implanted
0.316±0.007	0.355±0.004	0.383±0.001	0.381±0.001

of disorder [5], and only weakly depends on the doping (*n*- or *p*- type) [74]. In contrast, the intensity of the *G* band, which relates to the relative motion of sp^2 C atoms in the lattice, remains basically constant with increasing disorder in the low disorder regime, and then strongly decreases when graphene is turned into amorphous carbon [49]. Figure S5 shows the evolution of both $I_{\mathrm{D}}/I_{\mathrm{2D}}$ and $A_{\mathrm{D}}/A_{\mathrm{2D}}$ ratios. Unlike $I_{\mathrm{D}}/I_{\mathrm{G}}$ and $A_{\mathrm{D}}/A_{\mathrm{G}}$ ratios, which increase up to a maximum value and then decrease with increasing energy, $I_{\mathrm{D}}/I_{\mathrm{2D}}$ and $A_{\mathrm{D}}/A_{\mathrm{2D}}$ increase monotonically with increasing energy all the way up to 40 eV. This supports the notion that the rate of disorder formation increases monotonically with increasing implantation energy (at least up to 40 eV). However, we have observed that the intensity of the *2D* band can vary by a factor of 2 across a sample. Since this is also observed in our pristine Gr/Cu samples and is therefore unlikely to be a consequence of non-uniform ULE ion implantation. This variation in the *2D* band intensity is more likely associated with wrinkling (local strain relaxation [75]), defects of the Cu(111) film (*e.g.*, twin boundaries or surface roughness) and unintentional doping (*e.g.*, oxygen adsorption on graphene or copper oxidation [54, 76]).

3.3. XPS on Gr/Cu implanted with He, Ne and Ar at 25 eV

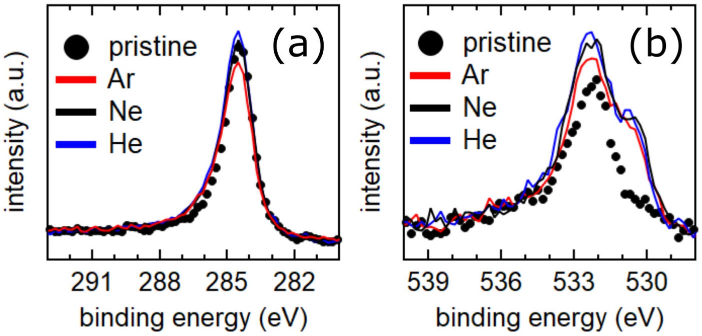

Figure S6. XPS spectra of C 1s (a) and O 1s (b) core-level peaks, measured on 25 eV noble gas implanted Gr/Cu, implanted with the following noble gases: (blue) He, (black) Ne, (red) Ar. Data for pristine Gr/Cu are shown (in black dots).

We also performed XPS measurements to quantify the amount of surface contamination induced by the ULE ion implantation process. Figure S6 shows the

XPS spectra near the C 1s and O 1s core-level peaks, for an implantation energy of 25 eV (chosen as a representative case). In the case of pristine Gr/Cu, the C 1s peak shows the typical asymmetric feature of sp^2 C; whereas the O 1s peak consists of two main components, located at $\approx$ 532.5 eV and $\approx$ 531 eV, which are both attributed to adventitious carbon (*i.e.*, carbon-oxygen (C-O) related bonding, due to air exposure) [38], which will be denoted as *type 1* and *type 2* adventitious carbon. Comparing implanted to pristine Gr/Cu, two main changes can be identified: for C 1s, there seems to be an additional component emerging at $\approx$ 286 eV, which is likely due to implantation-induced surface contamination or defects in graphene; for O 1s, the intensity of the *type 2* adventitious carbon increased by more than a factor of 2 after implantation. Interestingly, the changes induced upon implantation, in terms of the line shape, for both C 1s and O 1s, are essentially independent of which gas is implanted. An approximate quantification of C and O can be achieved assuming that the substrate, the Cu(111), consists of pure Cu, that is, C and O free. Table S1 shows the O/C ratio of pristine and implanted Gr/Cu: the O/C ratio varies between 0.316(7) for the pristine sample and 0.383(1) for the samples implanted with Ne. Although the implantation indeed led to an increase in the amount of some surface contamination, that effect is largely independent of the implanted element. On the other hand, as discussed in the main text, the amount of disorder inferred from the Raman spectroscopy data strongly increases with the atomic number of the implanted ion. In particular, for the implantation energy used for this XPS experiment (25 eV), the ratio of the D band versus G band is vanishingly small for He, and steadily increases from Ne to Ar (figure 9). Therefore we conclude that, although the surface modification induced by the ion implantation increases the surface reactivity of graphene, leading to a measurable increase in the amount of surface contamination, the latter does not scale with the amount of disorder.

3.4. XPS and Raman spectroscopy on Gr/Cu implanted with Ar at 40 eV

XPS was performed on the most defective (according to the Raman characterization) implanted graphene case, that is, implanted with Ar at 40 eV (figure S7). From the C 1s and O 1s peaks, a small increase in O/C ratio is observed (to 0.433(11), using the same quantification method as for table S1). Other than this slight increase, the effect of implantation is essentially the same as what is described in section 3. No indication of additional components is observed, for example, such as possible oxidation of Cu(111) substrate, which would otherwise indicate significant sputtering of the graphene layer. In figure S7c,d, showing the Cu 2p core-level peak and LMM Auger peaks, this Ar implanted Gr/Cu shows lower intensity in both spectra, implying that the higher disorder might have enhanced the surface reactivity of graphene (*e.g.*, at the defect sites), and therefore, the Cu signal in the spectra may be screened by the surface contamination. It is worth noting that judging from the line shape of the spectra, the Cu(111) still maintains a metallic signature, that is, remains protected

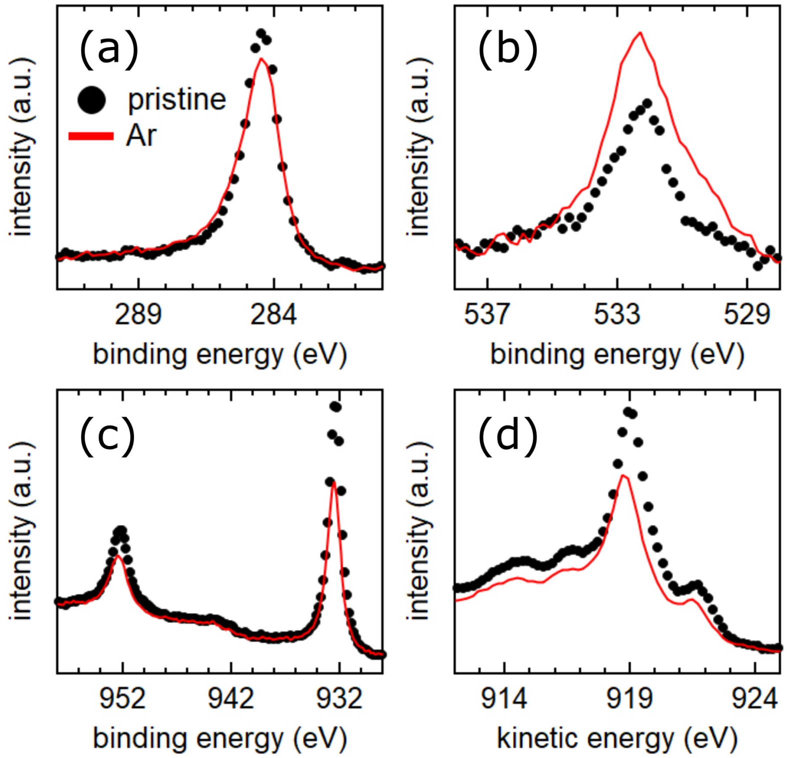

Figure S7. XPS spectra on pristine (black dots) and 40 eV Ar implanted (red line) Gr/Cu: (a) C 1s core-level; (b) O 1s core-level; (c) Cu 2p core-level; and (d) Cu LMM Auger.

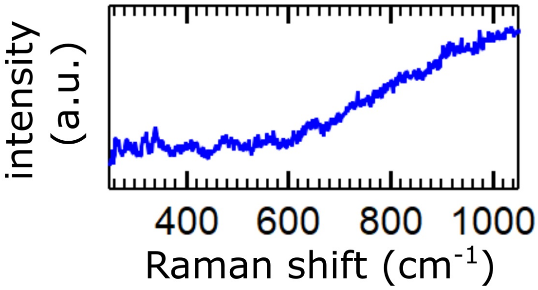

Figure S8. Raman spectrum for 40 eV Ar implanted Gr/Cu, in the region where copper oxide features would be observed if present.

from surface oxidation by the graphene layer [78, 79]. This is supported by the Raman data (figure S8), in which only the Cu photoluminescence background can be observed, without any indication of presence of copper oxide [58].

3.5. Disorder accumulation as a function of fluence: additional Raman analysis

Figure S9 shows the position of the *G* band, and in figure S9c, the FWHM of both the *G* and *2D* band are presented. In comparison to pristine Gr/Cu, mild amount of disorder (Γ_G increases from ≈12.5 cm^{-1} to ≈17 cm^{-1}) is observed on He implanted

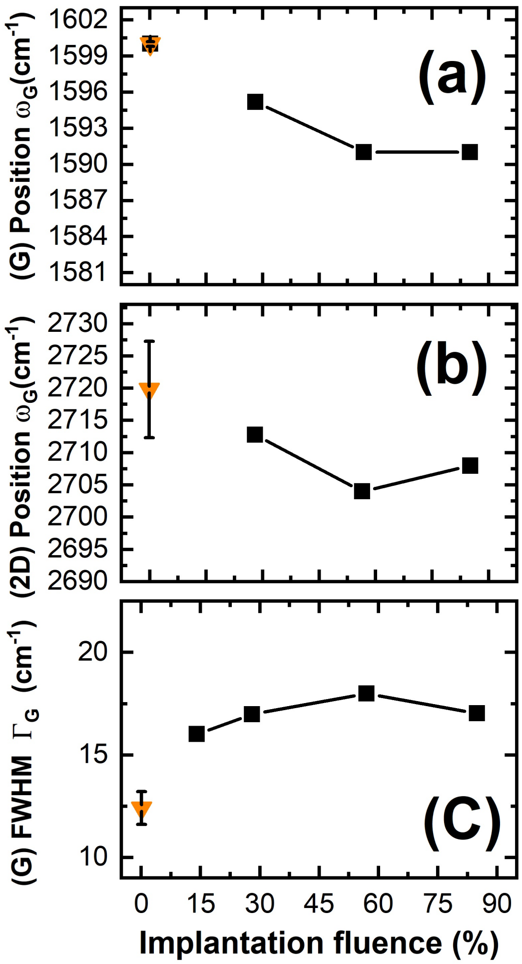

Figure S9. Positions of the *G* band (a) and *2D* band (b), and FWHM of the *G* band (c) for pristine graphene/Cu(111) (orange triangle) and as a function of the He fluence corresponding to 28%, 56% and 85% of the surface density of C in a graphene/Cu(111) layer.

Gr/Cu, as well as some tensile strain (red shift of both *G* and *2D* band), indicating the sp^2 bonds are broken by the ion implantation, and consequently weakly bonded to the underlying substrate [64]. The FWHM (Γ_G) stays below 18 cm^{-1} with an implantation concentration up to 85% (figure 11).